Supporting Information: Introducing functionalities into directly synthesised amorphous UiO-66-based metal-organic frameworks

Emily V. Shaw,[a] Javier Pérez-Carvajal,[b] Elena López-Elvira,[b] Shaoliang Guan,[a,c] Timothy Lambden,[a] Georgina P. Robertson,[a,d] Arad Lang,[a,c] Joonatan E. M. Laulainen,[a] Celia Chen,[a,c] Chumei Ye,[a,c] Anna Herlihy,[e] Catherine Dejoie,[d] David A. Keen,[f] Paul Midgley,[a] Thomas D. Bennett[a,g*] and Celia Castillo-Blas[a,b*]

a. Department of Materials Science & Metallurgy, University of Cambridge, 27 Charles Babbage Road, Cambridge, UK
b. Instituto de Ciencia de Materiales de Madrid (ICMM-CSIC), Sor Juana Inés de la Cruz 3, 28049, Madrid, Spain E-mail: castillo@icmm.csic.es
c. Maxwell Centre, Cavendish Laboratory, University of Cambridge, J. J. Thomson Avenue, Cambridge, CB3 0HE, UK.
d. ESRF - The European Synchrotron Radiation Facility, CS 40220, Grenoble, Cedex 9, 38043 France.
e. Diamond Light Source Ltd, Diamond House, Harwell Campus, Didcot, Oxfordshire, UK.
f. ISIS Facility, Rutherford Appleton Laboratory, Harwell Campus, Didcot, Oxfordshire OX11 0QX, UK
g. School of Physical and Chemical Sciences, University of Canterbury, Private Bag 4800, Christchurch 8140, New Zealand. E-mail: thomas.bennett@canterbury.ac.nz

Table of Contents

1. Synthetic Methods

Crystalline UiO-66, UiO-66-NH_2 and UiO-66-NO_2 were synthesised according to literature methodology.[1,2]

Amorphous UiO-66-Based materials were synthesised following a general procedure. The linkers used were terephthalic acid (UiO-66, 498 mg), 2-nitroterephthalic acid (UiO-66-NO_2, 633 mg) and 2-aminoterephthalic acid (UiO-66-NH_2, 650 mg).

4 mL of 1.0 M NaOH(aq) was added slowly to a suspension of 3 mmol Linker in 3.5 mL DI water and stirred for 30 mins. $ZrOCl_2.8H_2O$ (650 mg, 2 mmol) was dissolved in 4 mL DI water, added dropwise to the linker suspension, and stirred for 20 minutes. The resulting solid washed with DI water (3x20 mL) and EtOH (3x 20 mL) and activated at 150 °C under an active vacuum.

Milling of UiO-66 was carried out on evacuated powder samples. The sample was activated using a dynamic vacuum at 150 °C overnight. 120 mg was added to a 10 mL stainless steel jar, with 1x10 mm diameter stainless steel ball bearing (4.03 g) at room temperature. The jar was then milled at 30 Hz on a Retsch MM40 mixer mill for 30 minutes, the powder recovered and characterised.

Powder X-ray diffraction (PXRD) data were collected at room temperature using a Bruker D8 diffractometer using Cu Kα radiation (λ = 1.5418 Å). Scans were performed in Bragg-Brentano geometry over the scattering angle range $2° < 2\theta < 50°$. Pawley refinements were carried out using TOPAS Academic (V6) software.[3] The unit cell parameters were refined against those previously reported over the angular range $2° < 2\theta < 50°$.

Scanning Electron Microscopy (SEM) was performed using a FEI Nova NanoSEM operated at 5 keV for imaging using secondary electrons. Samples were prepared for SEM by securing to aluminium SEM pin stubs using carbon tape. Samples were coated in gold using an Emtech K575 sputter coater prior to imaging to prevent charging.

Scanning Electron Diffraction (SED) data was acquired on a TF Spectra 300 operated at 300 keV with a probe diameter of ca. 4 nm and a convergence angle of ca. 0.6 mrad. The current was 2 pA, and the data was acquired on a Merlin Medipix3 with a frame time of 1 ms, leading to an electron dose of ca. 10 $e^-/Å^2$. Data were collected at a camera length of 91 mm, and a C2 aperture of 30 µm. Diffraction and real-space calibration was performed using an AuPd grid. SED data were processed using pyxem.[4]

Thermogravimetric Analysis (TGA) was performed on a TA instruments SDT-Q600, under an air atmosphere, using a heating rate of 10 °C min^{-1}, from room temperature to 800 °C. An isotherm was performed at 100 °C for 10 minutes to ensure complete removal of solvent. Between 5-15 mg of activated sample was used for each measurement.

Fourier-Transformed Infrared Spectroscopy (FT-IR) data were collected on a Bruker Tensor 27. Data were collected in transmission mode between 600 and 4000 cm^{-1} through the use of an attenuated total reflectance cell. A background was collected and subtracted from all spectra, as well an atmospheric correction.

Elemental Analysis, CHN combustion analysis, was performed using a CE440 Elemental Analyser, EAI Exeter Analytical Inc. ~2 mg of sample was used for each run to give C, H and N % values.

Energy Dispersive X-ray Spectroscopy (EDS) data were collected on a Zeiss Gemini SEM, operated at 1.5 keV. Samples were spread on carbon tape and adhered to an SEM stainless steel stub. Sample quantification was done using Oxford Aztech software.

X-ray Total Scattering and Pair Distribution Function Analysis data were collected at beamline I15-1, Diamond Light Source, UK (CY39316-1) (CY31401-3) (λ = 0.161669 Å). A small amount of finely ground sample was loaded into a Kapton capillary (inner diameter of 0.5 mm) to a height of 1 cm. Capillaries were sealed and mounted onto the instrument. Data were collected at room temperature for each sample, an empty capillary and the blank instrument over the region $\sim 0.3 < Q < \sim 26$ Å^{-1}. The total scattering data were processed to account for absorption corrections and various scattering corrections (background scattering, multiple scattering, container scattering and Compton scattering) in a Q range of 0.25–18 Å^{-1}.

Data were also collected at beamline ID-22, European Synchrotron Radiation Facility (ESRF), Grenoble, France (MA-6548) (λ = 0.187796 Å). Ground sample was loaded into borosilicate capillaries (inner diameter of 0.7 mm) to a hight of 3 cm. Capillaries were sealed and mounted onto the instrument. Data were collected at room temperature for each sample, an empty capillary and the blank instrument. The total scattering data were processed to account for absorption corrections and various scattering corrections (background scattering, multiple scattering, container scattering and Compton scattering) in a Q range of 0.25–15 Å^{-1}.

Subsequent Fourier transformations of the processed total scattering data resulted in a real-space PDF $G(r)$ for each material. In this work, we use the $D(r)$ form of the PDF to accentuate high r correlations. All processing of the total scattering data was performed using GudrunX following well-documented procedures.[5–7]

Published structural models were refined against PDF data using PDFGui, producing partial PDFs for each correlation.[8] Values were initially set and fixed at r_{cut} = 5.75 Å and Q_{broad} = 0.0001. Q_{damp} = 0.08, data scale factor = 0.5 and model scale factor = 1.0 were utilised as starting values and then refined. Refinements were done in the range $0.5 < r < 10$ Å, with Q_{max} = 18 Å^{-1}. Thermal parameters were refined isotropically, defined initially as 0.0025 Å^2. Atomic positions were refined within appropriate symmetry constraints, defined by the space group, with limited variation observed from their starting positions. Structural models for the secondary building units (SBUs) were obtained from published crystalline models, with the model unit cell expanded to remove SBU-SBU correlations. Refinements were done in the range $0.5 < r < 10$ Å, with Q_{max} = 18 Å^{-1}.

Principal Component Analysis (PCA) were carried out on the $D(r)$ functions with Origin v2019 graphing software.[9] PCA is a dimensionality reduction technique, representing the patterns through weighted components. Principle components (PCs) were extracted, with the number of which equal to the number of data sets in the analysis. When PCA was conducted on the short-range order of the *a*MOF samples, the data were cut at 10 Å.

X-ray Photoelectron Spectroscopy (XPS) Analysis was performed using a Thermo NEXSA G2 XPS fitted with a monochromated Al kα X-ray source (1486.7 eV), a spherical sector analyser and 3 multichannel resistive plate, 128 channel delay line detectors. All data were recorded at 19.2W and an X-ray beam size of 400 x 200 µm. Survey scans were recorded at

a pass energy of 200 eV. Electronic charge neutralization was achieved using an ion source (Thermo Scientific FG-03). Ion gun current = 150 μA. Ion gun voltage = 40 V. All sample data were recorded at a pressure below 10-8 Torr and a room temperature of 294 K. Data were analysed using CasaXPS v2.3.26rev1.0N.

^{1}H Nuclear magnetic resonance spectroscopy (NMR) samples were prepared by base digesting the MOF (5-10 mg) in a solution of D2O (0.5 mL, 0.03% TMS) and NaOH/D_2O (0.1 mL) or D2SO4 (0.1 mL) and sonicated to encourage dissolution. Samples were run in a Bruker Advance III HD 500 MHz spectrometer. Spectra were calibrated using TMS as a standard. Analysis was performed using Mestrenova.

Gas Sorption was performed using an iQsorb instrument (Quantachrome), with nitrogen and CO_2 adsorption–desorption measurements were performed at 77 K and acetone at dry-ice temperature (195 K) respectively. Prior to the adsorption tests, samples were degassed under vacuum at 120◦C for 24 h. A specific region of the isotherms was fitted to the BET model to calculate the specific surface area of the porous solids, while the pore size distribution was determined by the DFT method using the instrument software. Pore size distribution is derived from nitrogen adsorption isotherms applying DFT method from iQsorb instrument sotfware (ASQiWin®). Total pore is calculated form each CO_2 adsorption isotherm collected at 195 K at the pressure of 720 torr.

Heat of adsorption ($\Delta_{ads}H$) of CO_2 was calculated according to Clausius-Clapeyron Equation (Equation S1).

$$\Delta_{ads}H = -R \ln\left(\frac{P_2}{P_1}\right)\frac{T_1.T_2}{T_2 - T_1} \qquad Eq.S1$$

CO_2 isotherms at 273 and 298 K were sequentially collected on each material from vacuum to 1 bar using an iQsorb instrument (Quantachrome). Prior to measurements samples were degassed under vacuum at 120◦C for 24 h. Data collected from each pair of temperatures are derived at constat CO_2 loading to determine the heat of adsorption values.[10]

Catalytic Activity Testing: Levulinic Acid Esterification. A glass reaction vial was charged with 1 mmol Leuvelinic Acid, 5 mmol Solvent (EtOH or MeOH), and 1% Catalyst (wrt Leuvelinic Acid). The vial was sealed with a pressure seal, and heated under vigorous stirring for 3h and 120 °C. The catalyst was separated vial filtration, and washed in EtOH (3x 5mL) and reactivated in a vacuum oven at 150 °C overnight.

Gas Chromatography (GC) analysis was performed using a KONIK IPGC 5000 equipped with a flame ionisation detector; with a KAP-120212 capillary column (30 m, 0.25 mm, 0.25 μm). Samples were diluted in acetone before 1 μL of the sample was injected, with an injector temperature of 250 ˚C. The oven had an initial temperature of 60 ˚C, with a delay of 3 minutes, before heating at 10 ˚C min^{-1} to 250 ˚C. The detector was held at 280 ˚C. Analytes were carried through the column with nitrogen as the carrier gas, at a constant flow rate of 2.5 barr. Peak identification was performed by comparison to known materials. Quantification of peak area was performed using KonikKROM Plus software.

^{1}H Nuclear magnetic resonance spectroscopy (NMR) samples were collected in a Bruker 300 AV spectrometer operating at 300 MHz using $CDCl_3$ as the NMR solvent.

pH Testing was performed following literature methodology.[11] 3 mg of the MOF was dispersed in 9 mL of methanol and kept under stirring for 3 h at room temperature before pH measurements. pH was measured using a HI 2212 pH meter.

Far Infrared (Far-IR) data were collected using a Bruker Vertex 70V Spectrophotometer with microscope Hyperion 2000 operating in a spectral range from 50 to 18000 cm-1. Samples were prepared dispersing a small amount (~ 1 mg) in CsI to prepare a 13mm pellet.

2. a_SUiO-66

2.1. Powder X-Ray Diffraction

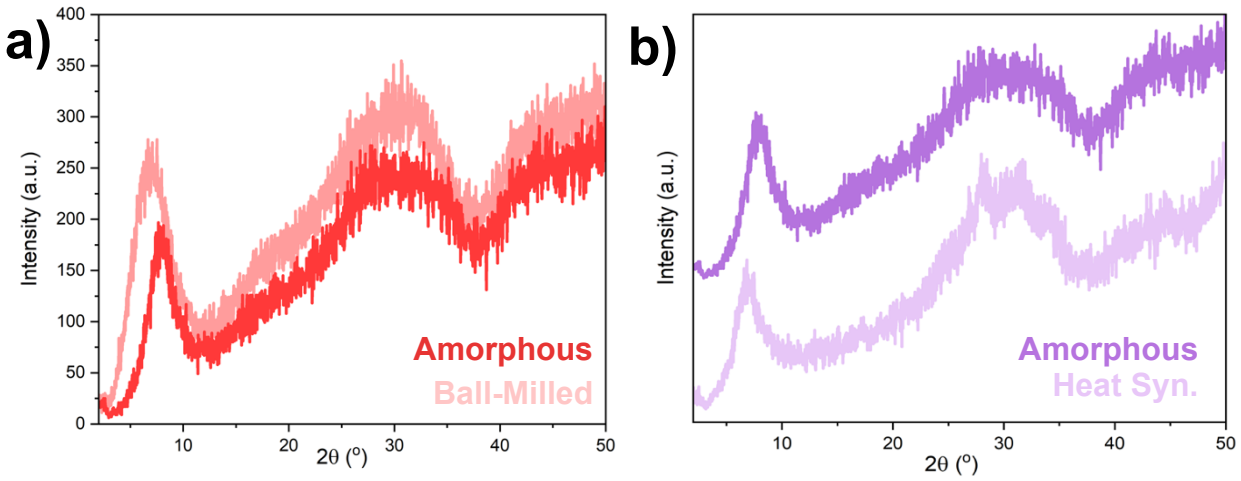

Figure S1: a) PXRD of directly synthesised (a_S-, red) and ball-milled (a_m-, light red) amorphised UiO-66. B) PXRD of a_sUio-66 prepared at room temperature (light purple) and after heating at 180 °C for 24h (dark purple). Data were offset for clarity. Wavelength = 1.54056 Å.

2.2. Scanning Electron Microscopy

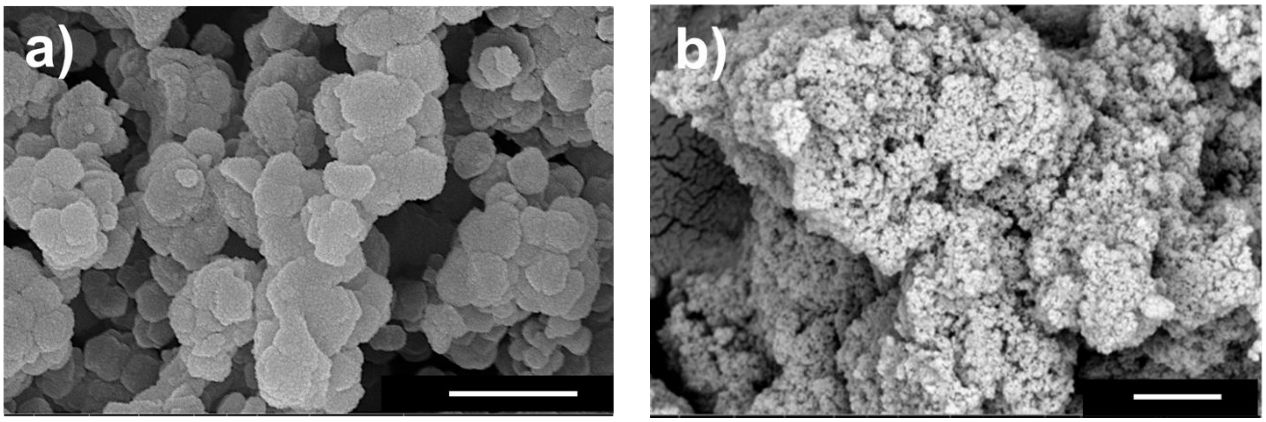

Figure S2: SEM images of a) crystalline and b) amorphous UiO-66. Scale-bar = 500 nm.

2.3. Fourier-Transform Infrared Spectroscopy

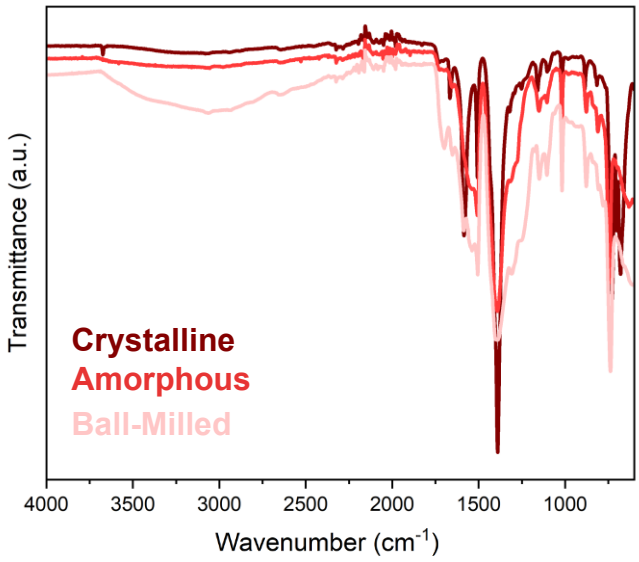

Figure S3: Full FT-IR spectra UiO-66 (dark red), a_sUiO-66 (red) and a_mUiO-66 (light red).

Table S1: Key vibrational assignments of UiO-66, from FT-IR spectra, **Fig. S2**. Extracted using Fityk.[12]

	PEAK POSITION / cm^{-1}			PEAK AREA / a.u.		
	CRYST.	***a*s**	***a*m**	**CRYST.**	***a*s**	***a*m**
C-O VIB. (ASYMMETRIC)	1507, 1570	1506, 1567	1504, 1586	258, 854	345, 914**	472, 1627**
C-O VIB. (SYMMETRIC)	1390	1390	1386	2671	3010	2460
MONO-COORDINATED C-O VIB.	N/A	1528	1533	N/A	533	1060

** Overlap between monocoordinated and dicoordinated vibrations, limiting the accuracy of these values.

2.4. Thermogravimetric Analysis

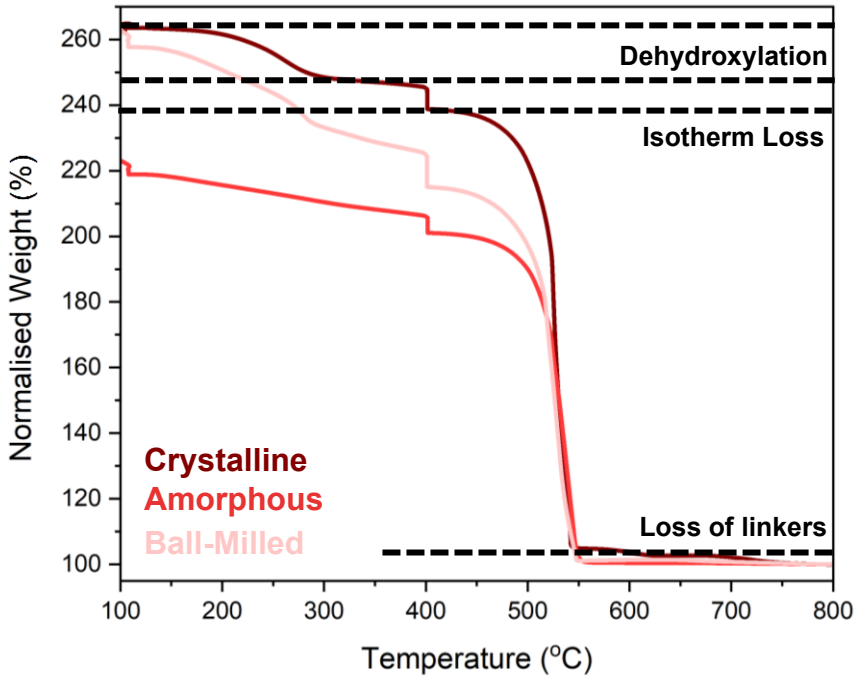

Figure S4: TGA of UiO-66 (dark red), a_sUiO-66 (red) and a_mUiO-66 (light red). 30 minute isotherms were performed at 100 °C, corresponding to the removal of solvent, and 400 °C. The weight loss observed at 400 °C was as a result of the loss of mon°Coordinated linker from performing the isotherm. Labels correspond to the end point of key weight losses of the crystalline material.

2.5. Compositional Analysis

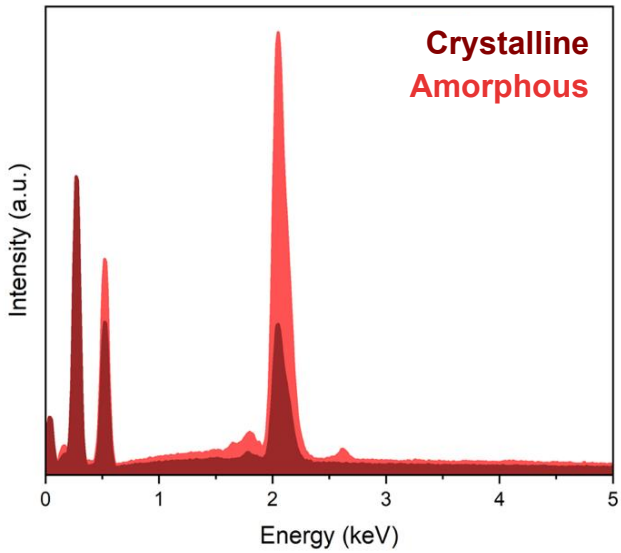

Figure S5: EDX spectra for directly synthesised amorphous (red) and crystalline (dark red) UiO-66.

Table S2: EDX compositional analysis

	Crystalline (%wt)	***Amorphous (%wt)***
O	61.06 ± 0.45	47.74 ± 0.35
Zr	38.94 ± 0.45	51.35 ± 0.35
Cl	0	0.91 ± 0.08

Table S3: Compositional Analysis determined from TGA and EDX. The amount of DMF retained within the structure was determined from %N from the experimental CHN. Discrepancies in the CHN was attributed to the presence of water bound to the structures.

	Experimental Composition	Theoretical CHN	Experimental CHN
Crystalline	$Zr_6O_4(OH)_4(C_8H_4O_6)_6(C_3H_7NO)_{1.3}(H_2O)_4$	C: 30.8%, H: 2.25%, N: 0.90%	C: 33.04%, H: 3.98%, N: 0.95%
Ball-Milled	$Zr_6O_4(OH)_4(C_8H_4O_6)_{5.84}(C_8H_5O_6)_{0.16}(C_3H_7NO)_{1.44}(H_2O)_2$	C: 31.5%, H: 2.13%, N:1.01%	C: 32.77%, H: 2.65%, N: 1.02%
Amorphous	$Zr_6O_{4.7}(OH)_{3.3}(C_8H_4O_6)_{5.45}(C_8H_5O_6)_{0.2}Cl_{0.5}(H_2O)_6$	C: 28.4%, H: 2.01%, N: 0.00%	C: 30.44%, H: 2.19%, N: 0.00%

2.6. Total Scattering and Pair Distribution Function Analysis

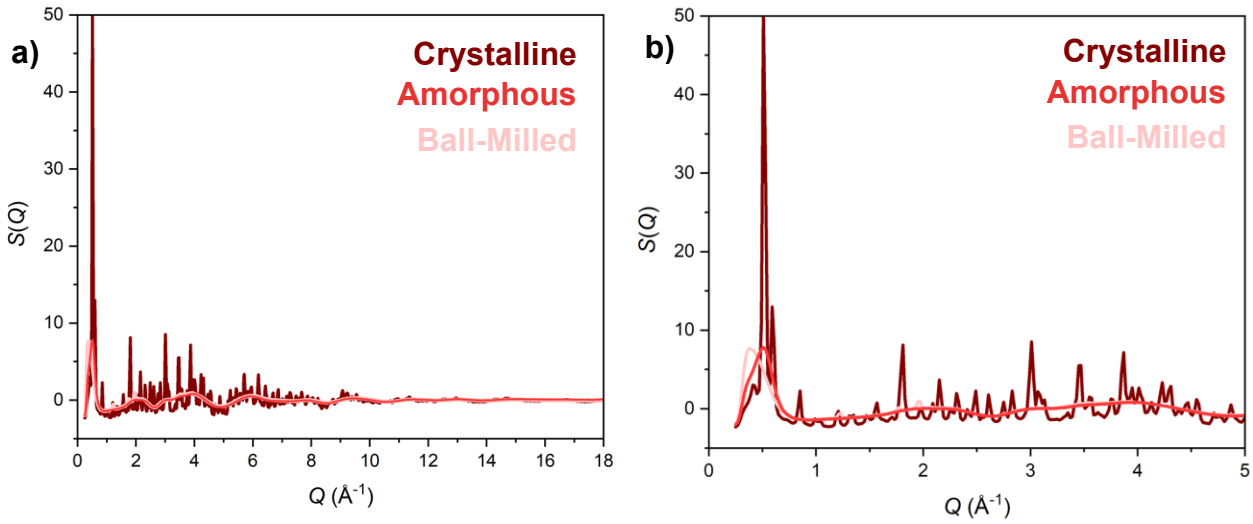

Figure S6: X-ray total scattering structure factors, *S*(*Q*), for the UiO-66 materials, a) whole range, b) narrow range.

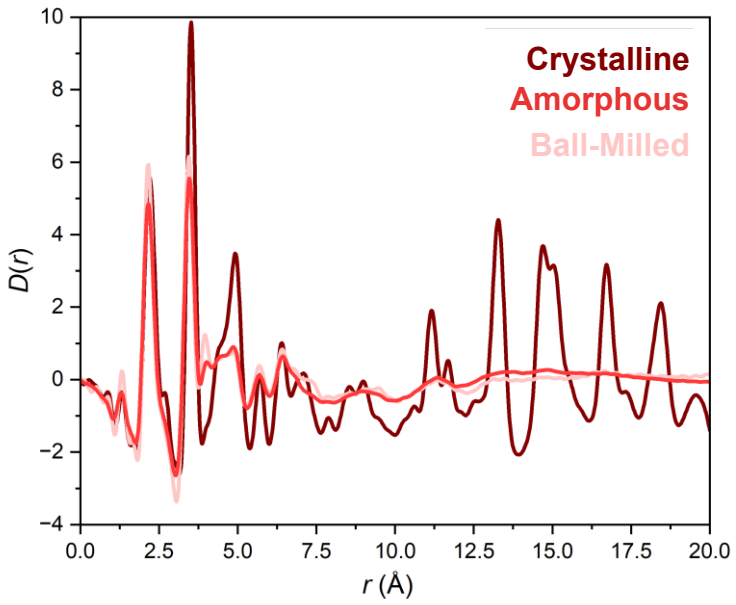

Figure S7: Pair distribution functions for the UiO-66 materials.

Table S4: Key contributions to each marked PDF peak, **Fig. 4**.

PEAKS		CONTRIBUTIONS	
LABEL	**PEAK POSITION**	**LINKER BASED**	**SBU**
A	1.36	C-C	-
B	2.18	O-C	O-Zr, O-O
C	2.72	C-O, Zr-C	O-O
D	3.29	Zr-C	Zr-Zr, Zr-O
E	4.42	O-O	O-O, Zr-O
F	4.94	Zr-C, O-O	Zr-Zr, Zr-O
G	5.70	Zr-C	O-O, Zr-O
H	6.40	Zr-C, O-C	O-O
J	7.14	Zr-C, C-O	-

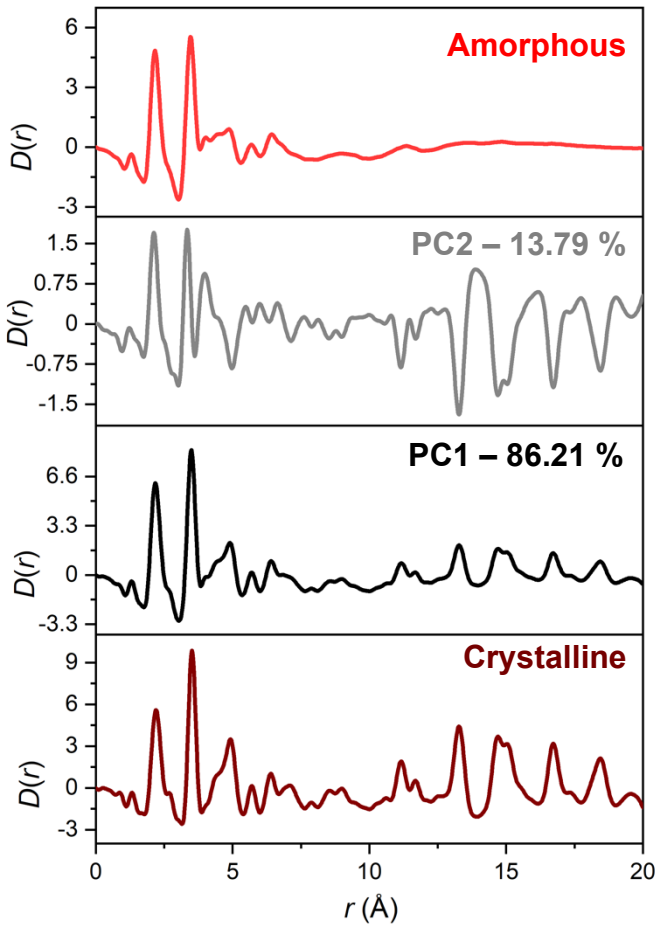

Figure S8: a) Principal component analysis with % variance values of 86.21 and 13.79% for PC1 and PC2 respectively, with comparison to crystalline and amorphous UiO-66. Eigenvalues were 1.72 and 0.28 respectively.

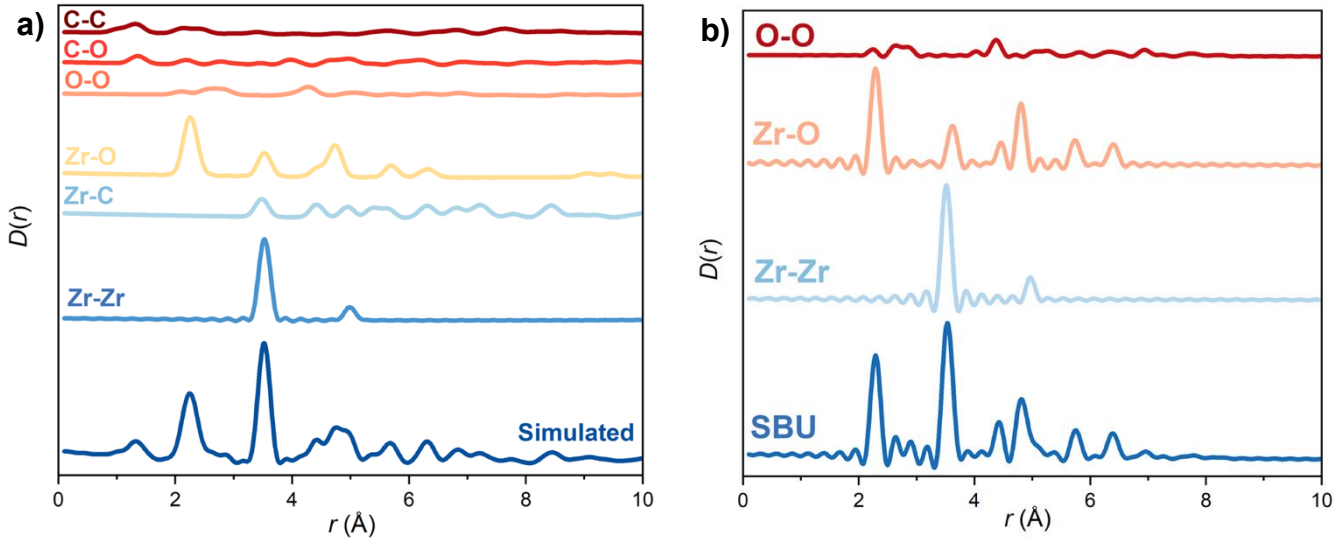

Figure S9: Partial PDF of a) whole structure and b) SBU-isolated structure, displaying idealised correlation length scales.

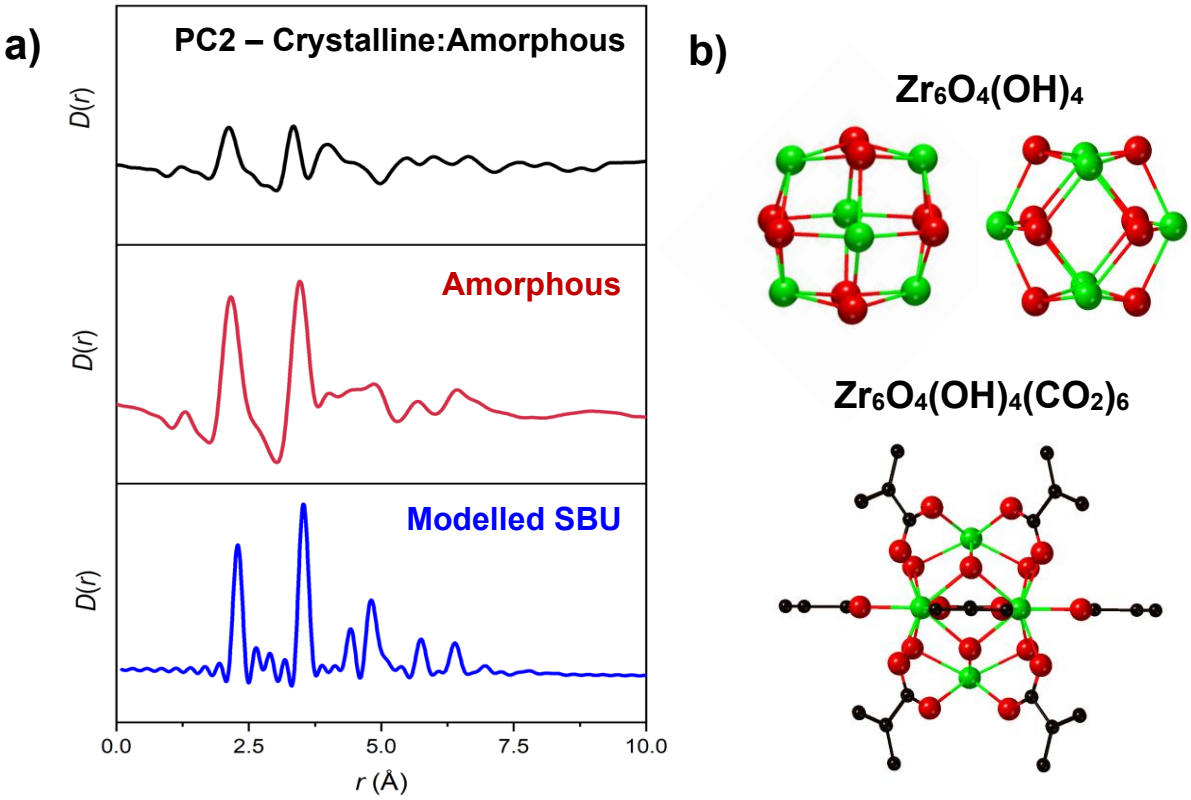

Figure S10: a) Simulated pair distribution function of the secondary building unit, compared to the experimental *a*$_s$UiO-66 spectra and the PC2, the difference spectra, of crystalline and amorphous UiO-66. Simulated spectra do not contain hydrogen-based contributions. b) UiO-66 $Zr_6O_4(OH)_4$ SBU structure. Structures calculated from a reported crystal structure.[13]

2.7. a_sUiO-66 Additives

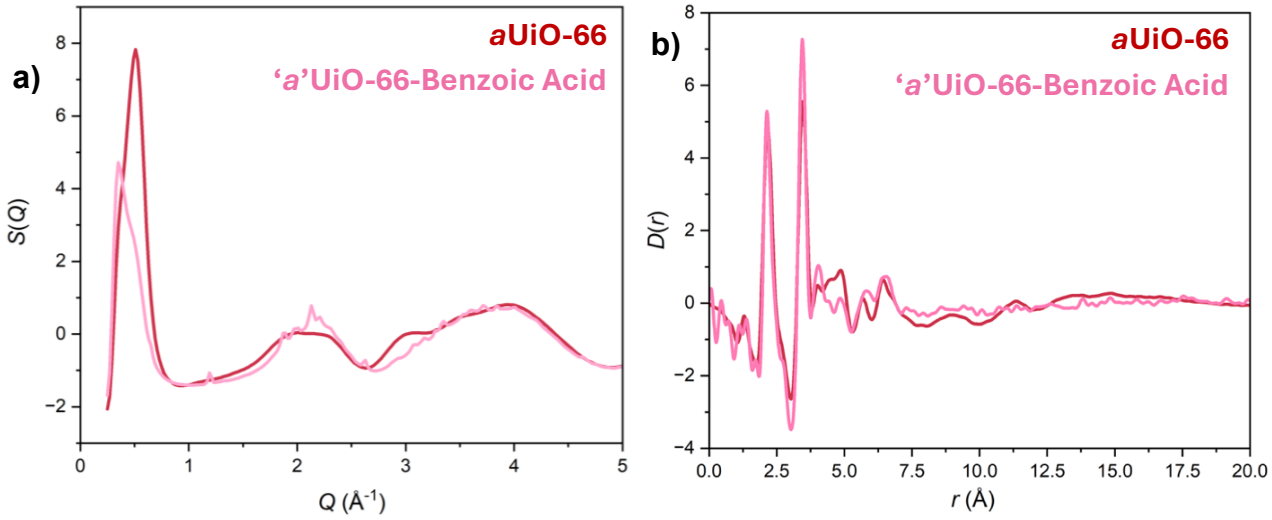

Figure S11: a) Total scattering and b) PDF analysis of a_sUiO-66 (red) and 'a_s'UiO-66-Benzoic Acid (pink). Data were collected at I-151 beamline (wavelength = 0.161669 Å). The benzoic acid sample is denoted 'a' due to the presence of a degree of crystallinity in the supposedly amorphous sample.

2.8. X-ray Photoelectron Spectroscopy

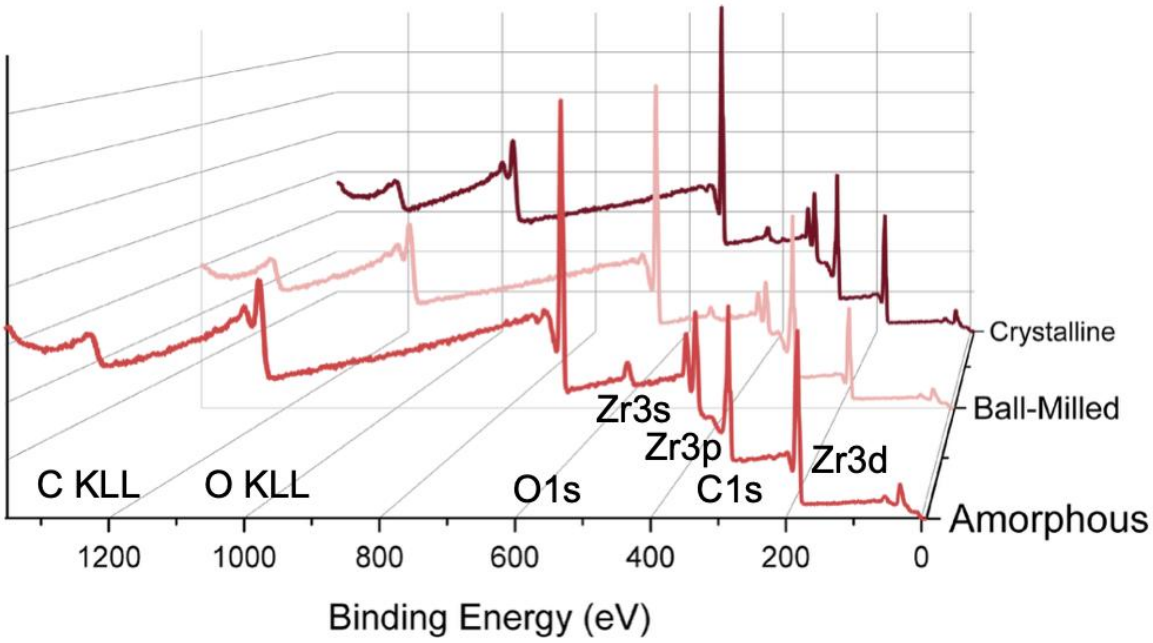

Figure S12: XPS survey of crystalline (dark), ball-milled (light) and amorphous (red) MIL-125-NH_2.

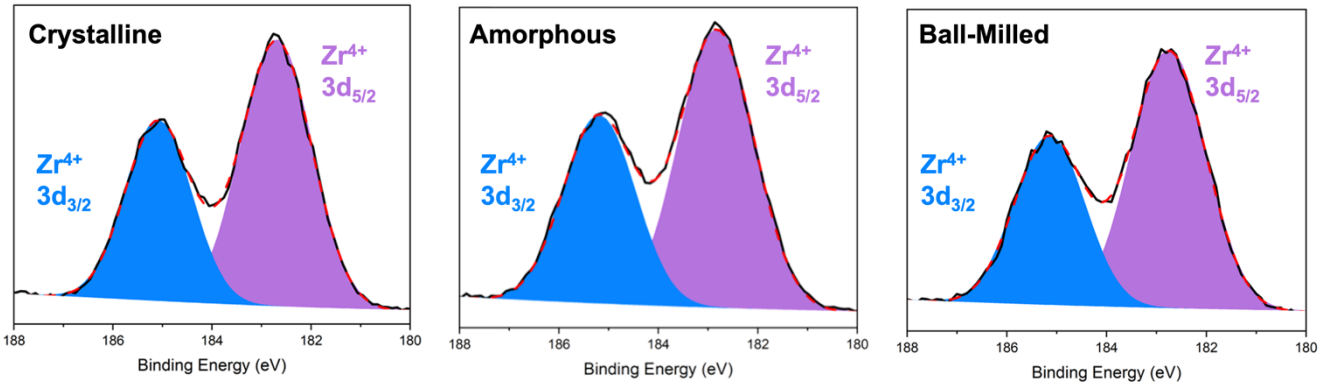

Figure S13: 3d Zr XPS spectra for various states of UiO-66 with deconvoluted contributions labelled.

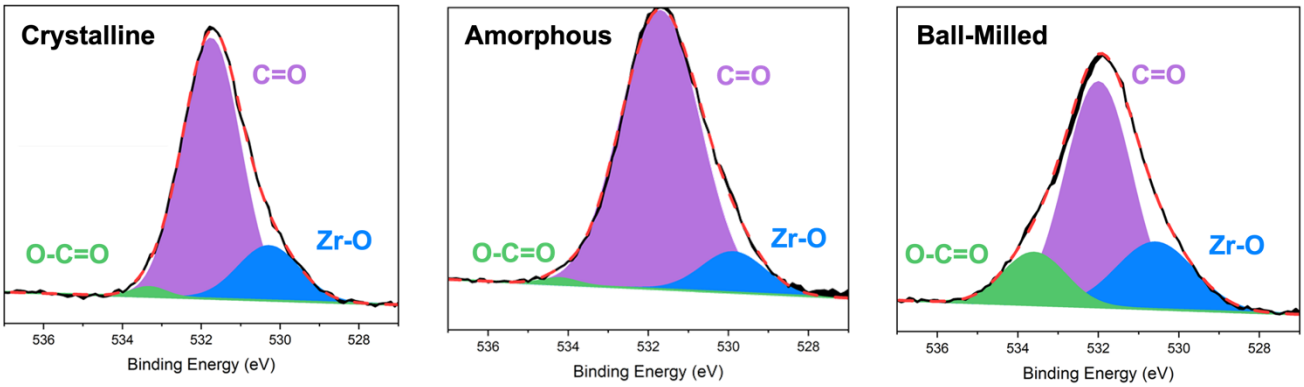

Figure S14: 1s O XPS spectra for various states of UiO-66 with deconvoluted contributions labelled.

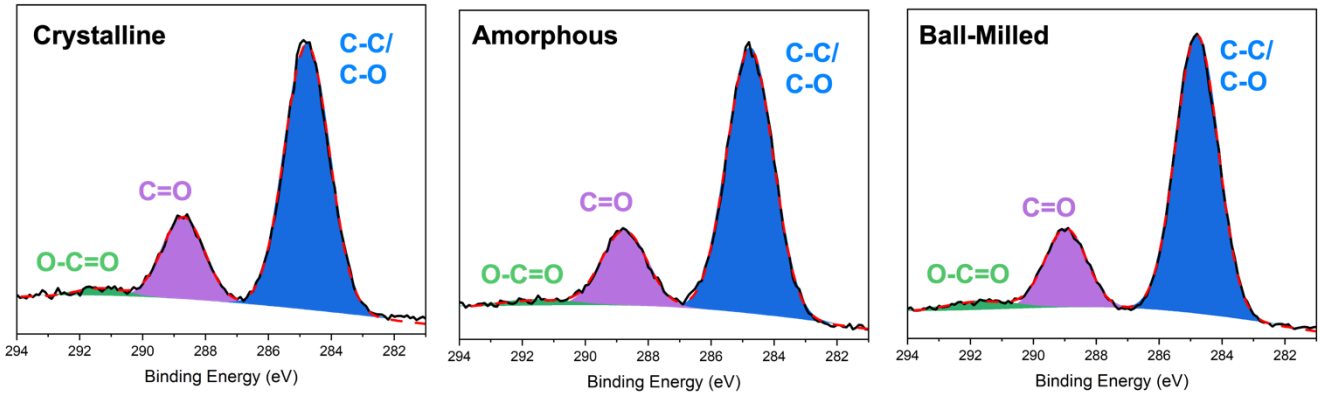

Figure S15: 1s C XPS spectra for various states of UiO-66 with deconvoluted contributions labelled.

Table S5: Summary of the fittings of the deconvoluted contributions from Figures S13, S14, S15, extracted using Fityk.[12]

	PEAK POSITION / eV			PEAK AREA / *a.u.*			RELATIVE PEAK AREA*		
	CRYST.	a_s	a_m	CRYST.	a_s	a_m	CRYST.	a_s	a_m
$3d_{5/2}$	182.7	182.8	182.8	5200	6891	3687	1	1	1
$3d_{3/2}$	185.1	185.1	185.2	8205	10688	5984	1.58	1.55	1.62
Zr-O	530.3	530.9	530.6	4958	3682	7382	0.95	0.53	2.00
C=(O)	531.8	531.7	532.0	22434	31838	21087	4.31	4.62	5.72
(O)-C=O	533.3	534.2	533.6	475	310	4654	0.09	0.04	1.26
C-C/C-O	284.8	284.8	284.8	10835	11997	13970	2.08	1.74	3.79
(C)=O	288.7	288.6	289.0	3155	3354	3808	0.61	0.49	1.03
O-(C)=O	291.3	291.6	291.7	368	454	711	0.07	0.07	0.19

3. a_SUiO-66-X MOFs

3.1. Pawley Refinements

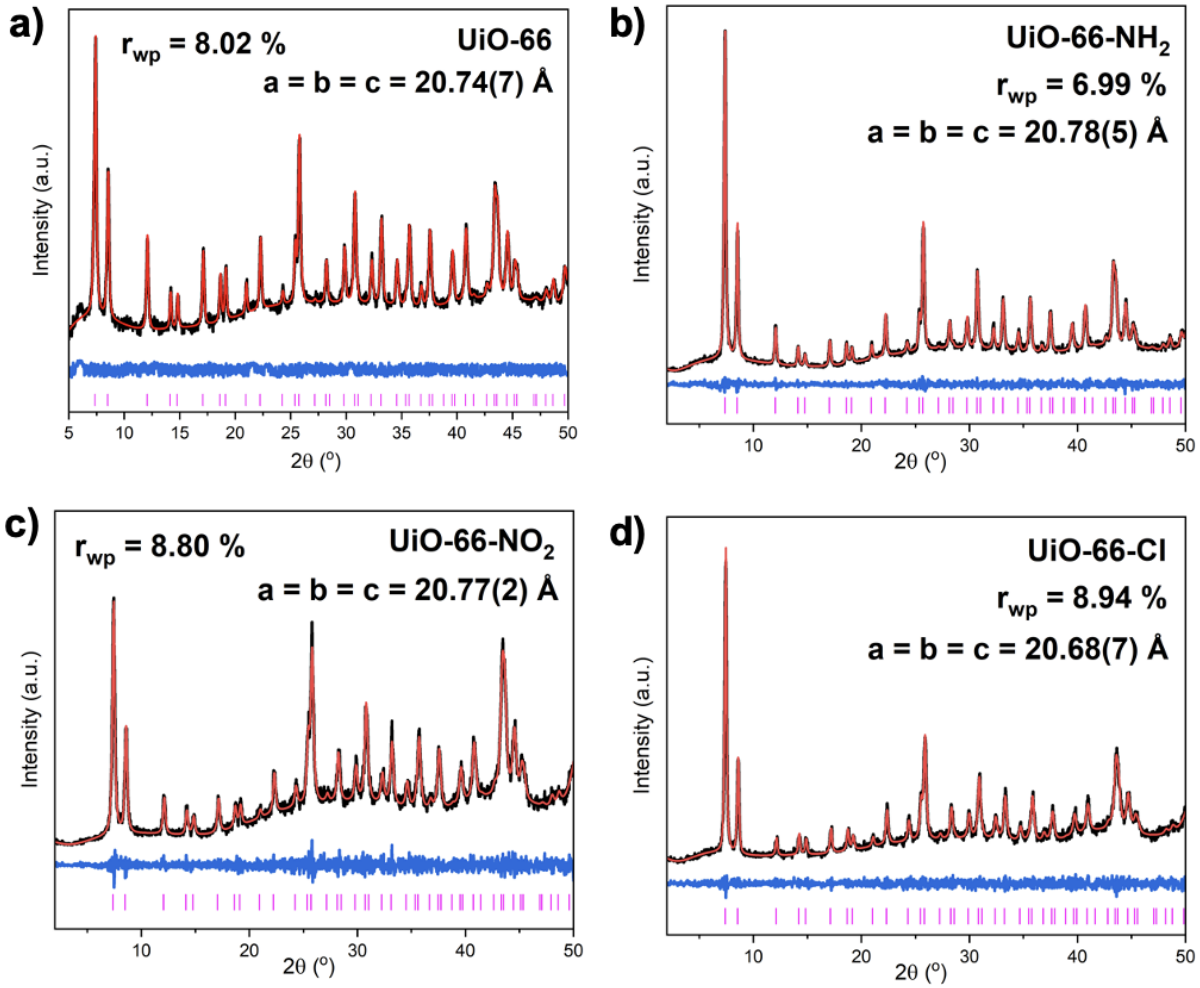

Figure S16: Pawley refinements for a) UiO-66, b) UiO-66-NH_2, c) UiO-66-NO_2 and d) UiO-66-Cl. Experimental data (black), calculated diffraction pattern (red), difference function (blue) and symmetry-allowed reflections (pink). Symmetry allowed reflections were calculated from the reported crystallographic information file.[13]

3.2. Scanning Electron Microscopy

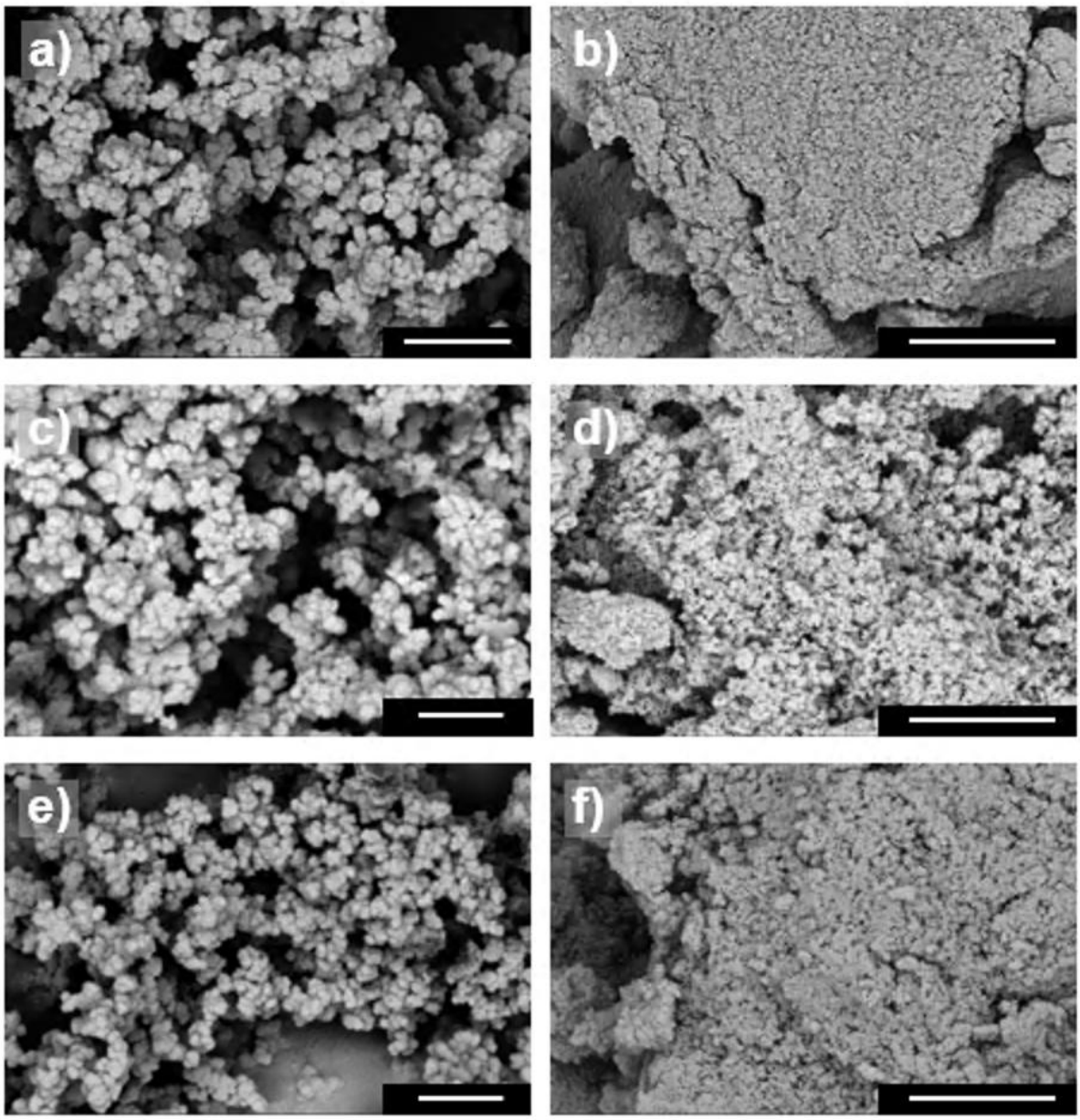

Figure S17: SEM images of a) UiO-66-NH_2, b) a_sUiO-66-NH_2, c) UiO-66-NO_2, d) a_sUiO-66-NO_2, e) UiO-66-Cl, f) a_sUiO-66-Cl. Scale-bar = 1 µm.

3.3. Linker Incorporation

Table S6: Key vibrational assignments of UiO-66-X, from FT-IR spectra, **Fig. S18**. Extracted using Fityk.[12]

	Peak Position / cm^{-1}					
	UiO-66-NH_2		**UiO-66-NO_2**		**UiO-66-Cl**	
	Cryst.	**Amorph.**	**Cryst.**	**Amorph.**	**Cryst.**	**Amorph.**
CO Vib. (Asymmetric)	1495, 1576	1494, 1544	1496, 1593	1495, 1595	1487, 1594	1489, 1561
CO Vib. (Symmetric)	1380	1380	1388	1392	1397	1392
Functionality	1254, 1429	1251, 1431	1535	1534	1051	1051

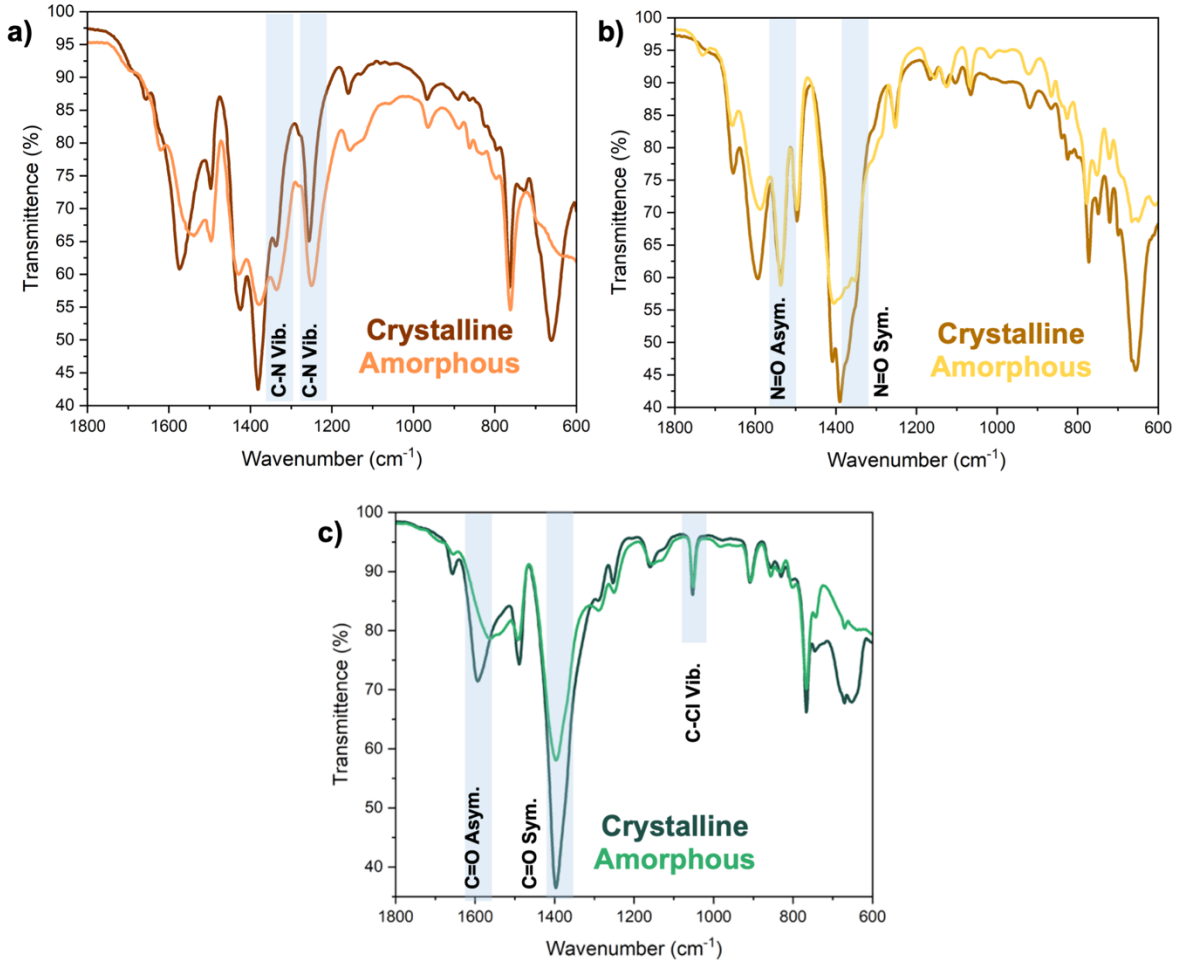

Figure S18: FTIR of crystalline (dark) and a_sMOF (light) for a) UiO-66-NH_2, b) UiO-66-NO_2 and c) UiO-66-Cl.

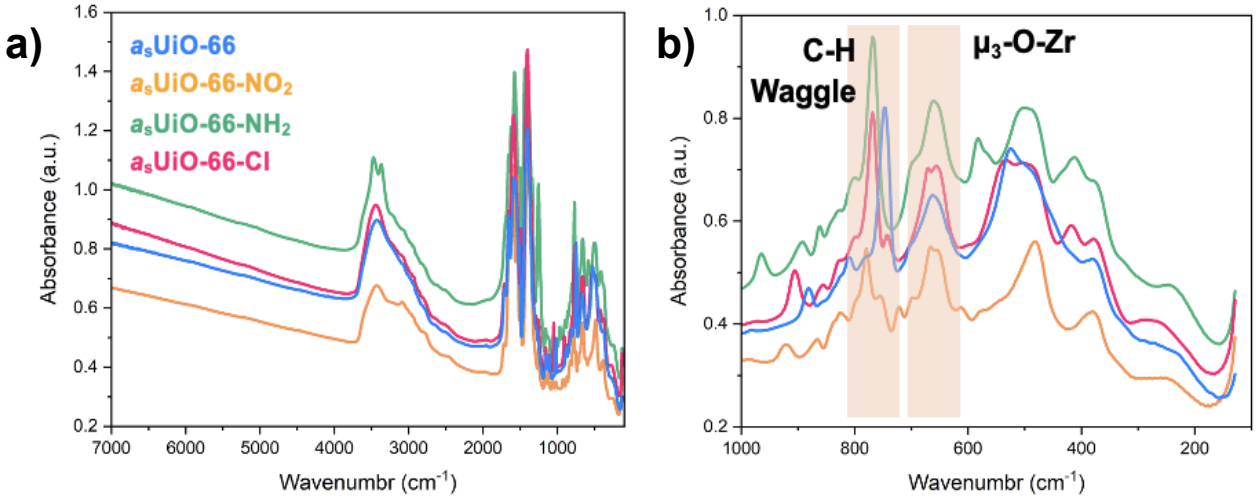

Figure S19: Far infrared spectroscopy of a_sUiO-66 (blue), a_sUiO-66-NH_2 (green), a_sUiO-66-NO_2 (orange) and a_sUiO-66-Cl (pink) c) full spectra, d) low-wavenumber region.

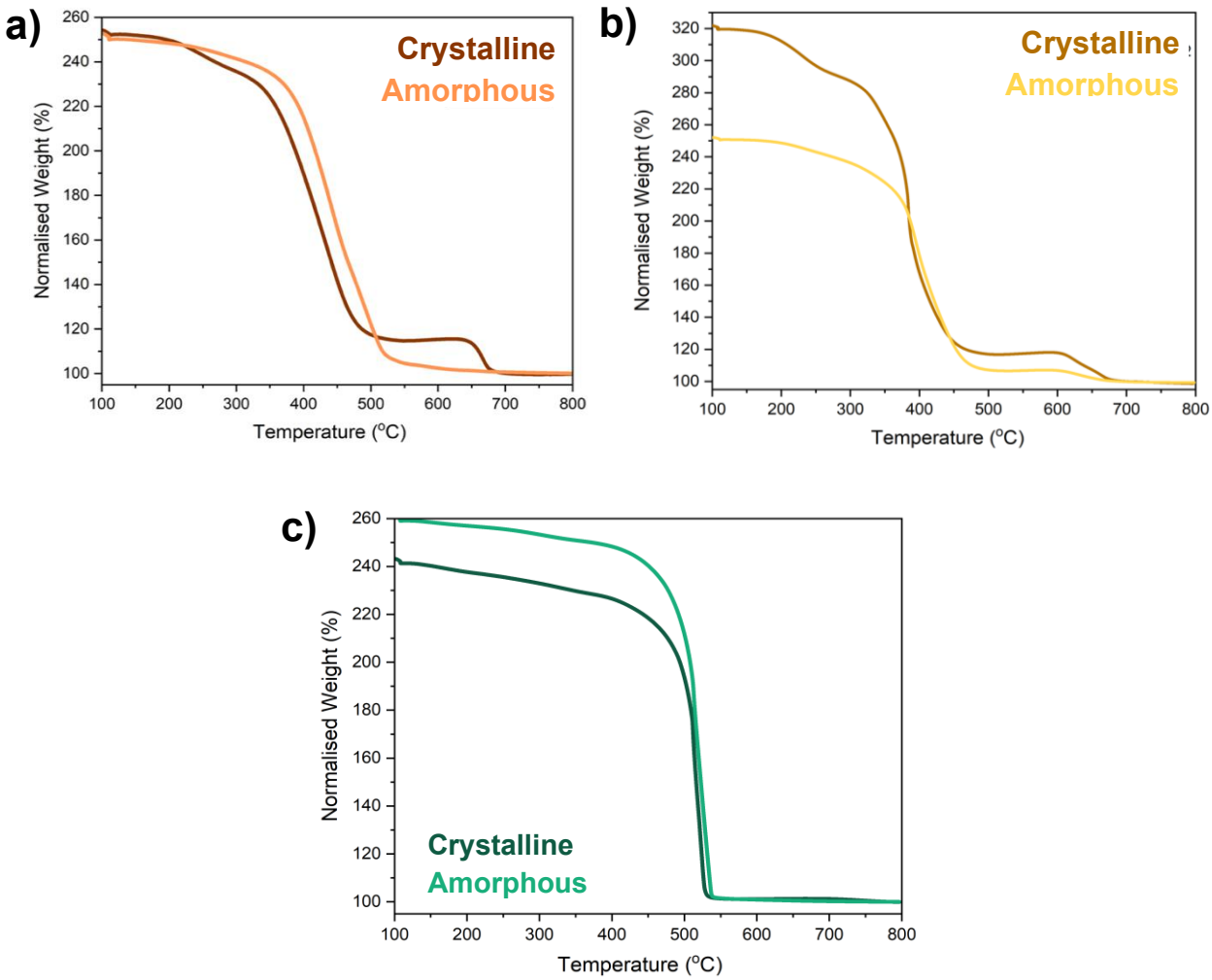

Figure S20: TGA crystalline (dark) and amorphous (light) a) UiO-66-NH_2 b) UiO-66-NO_2, and c) UiO-66-Cl.

Table S7: Compositional Analysis determined from TGA and EDX. The amount of DMF retained within the structure was determined from %N from the experimental CHN. Discrepancies in the CHN was attributed to the presence of water bound to the structures. DMF contamination noted from the lab.

		Composition	Theoretical CHN	Experimental CHN
UiO-66-NH_2	Cryst.	$Zr_6O_4(OH)_4(C_8H_4O_6)_6(C_3H_7NO)_{1.3}(H_2O)_4$	C: 30.8%, H: 2.25%, N: 0.90%	C: 29.24%, H: 4.43%, N: 4.18%
	Amorph.	$Zr_6O_4(OH)_4(C_8H_4O_6)_{5.84}(C_8H_5O_6)_{0.16}(C_3H_7NO)_{1.44}(H_2O)_2$	C: 31.5%, H: 2.13%, N:1.01%	C: 3.35%, H: 2.65%, N: 4.88%
UiO-66-NO_2	Cryst	$Zr_6O_{4.7}(OH)_{3.3}(C_8H_4O_6)_{5.45}(C_8H_5O_6)_{0.2}(C_3H_7NO)_{0.4}Cl_{0.5}(H_2O)_6$	C: 28.7%, H: 2.12%, N: 0.29%	C: 30.58%, H: 2.55%, N: 5.29%
	Amorph.	$Zr_6O_4(OH)_4(C_8H_4O_6)_6(C_3H_7NO)_{1.3}(H_2O)_4$	C: 30.8%, H: 2.25%, N: 0.90%	C: 29.2%, H: 2.06%, N: 4.64%
UiO-66-Cl	Cryst.	$Zr_6O_4(OH)_4(C_8H_4O_6)_{5.84}(C_8H_5O_6)_{0.16}(C_3H_7NO)_{1.44}(H_2O)_2$	C: 31.5%, H: 2.13%, N:1.01%	C: 32.77%, H: 2.65%, N: 1.02%
	Amorph.	$Zr_6O_{4.7}(OH)_{3.3}(C_8H_4O_6)_{5.45}(C_8H_5O_6)_{0.2}(C_3H_7NO)_{0.4}Cl_{0.5}(H_2O)_6$	C: 28.7%, H: 2.12%, N: 0.29%	C: 29.08%, H: 2.17%, N: 0.30%

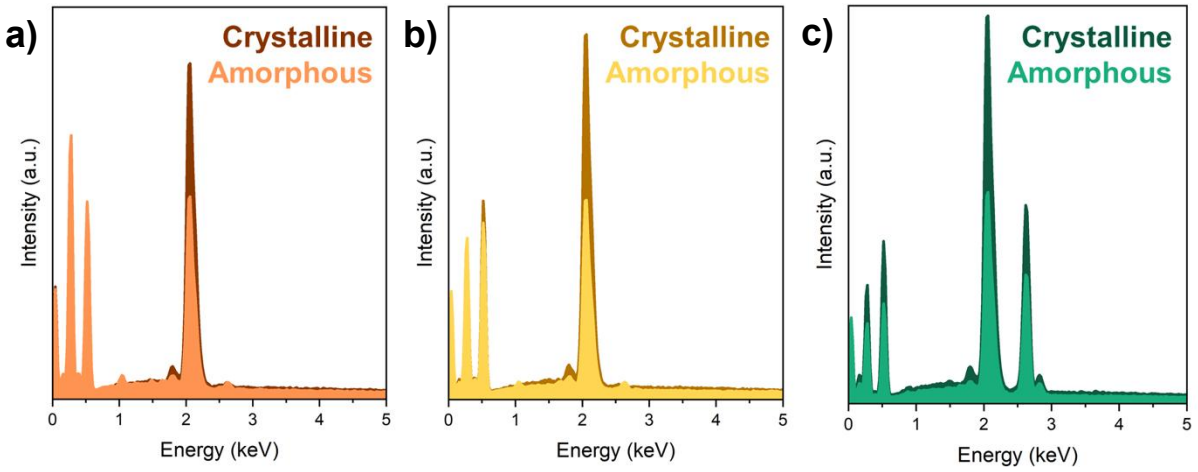

Figure S21: EDX spectra for directly synthesised amorphous (light) and crystalline (dark) a) UiO-66-NH_2, b) UiO-66-NO_2 and c) UiO-66-Cl.

Table S8: EDX compositional Analysis. *Na contamination, 1.16 ± 0.37 and 0.69 ± 0.1 respectively.

	UiO-66-NH_2		***UiO-66-NO_2***		***UiO-66-Cl***	
	Crystalline (%wt)	**Amorphous (%wt)***	**Crystalline (%wt)**	**Amorphous (%wt)***	**Crystalline (%wt)**	**Amorphous (%wt)**
O	41.14 ± 1.96	53.34 ± 5.96	49.86 ± 1.88	54.30 ± 1.60	40.08 ± 1.50	46.64 ± 5.02
Zr	50.37 ± 2.42	40.87 ± 6.14	47.36 ± 2.07	40.38 ± 1.86	44.18 ± 1.13	38.10 ± 3.81
Cl	0.17 ± 0.08	1.02 ± 0.14	0	1.05 ± 0.08	15.75 ± 0.59	15.59 ± 1.30

3.4. Total Scattering and Pair Distribution Function Analysis

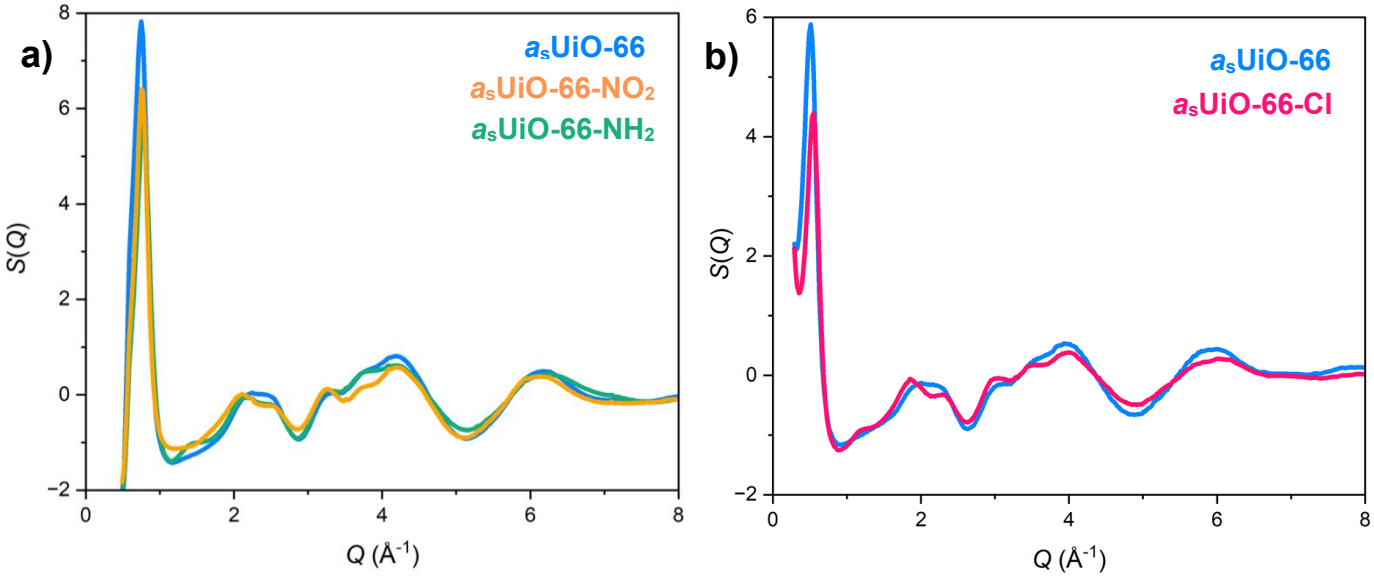

Figure S22: Narrow total scattering data collected at a) Diamond and b) ESRF.

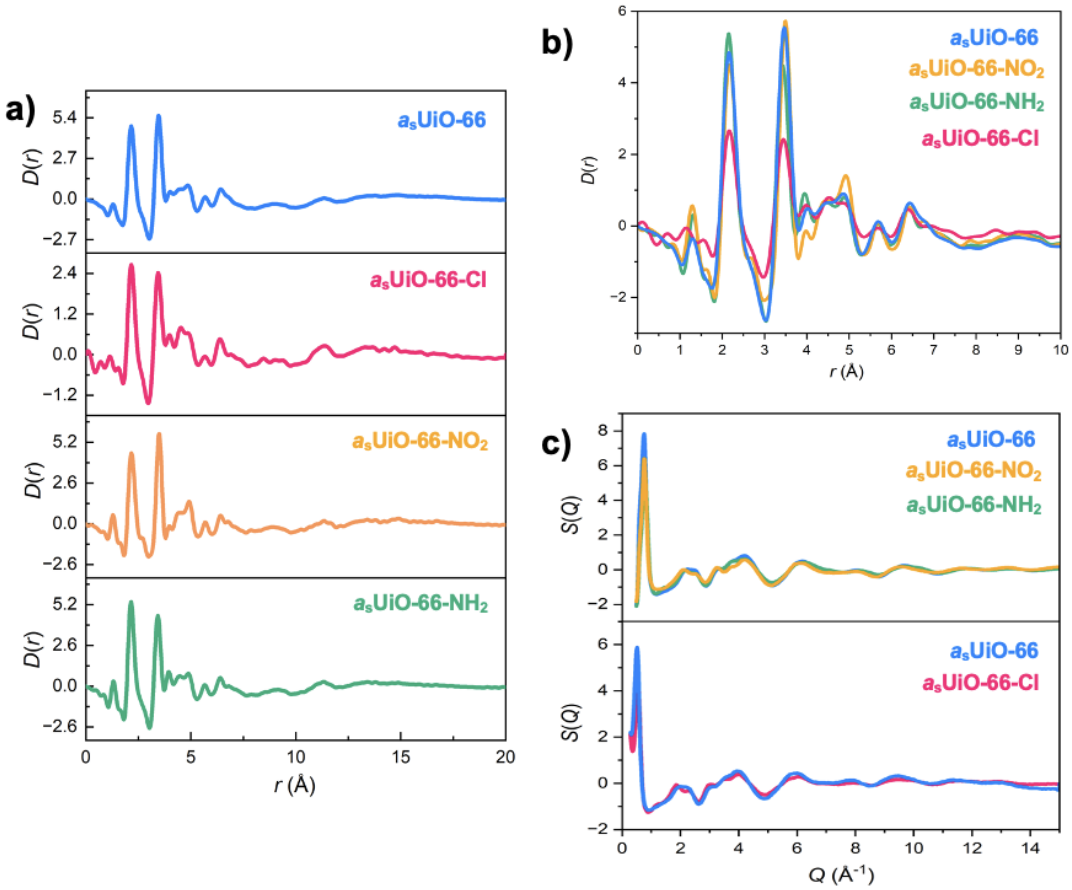

Figure S23: a) Wide PDF spectra for *a*$_s$UiO-66-based MOF materials. B) Stacked PDF data for *a*UiO-66-X materials. c) Wide total scattering data for *a*$_s$MOFs collected at Diamond I15-1 (top) and ESRF (bottom).

4. Applications

4.1. Gas Sorption:

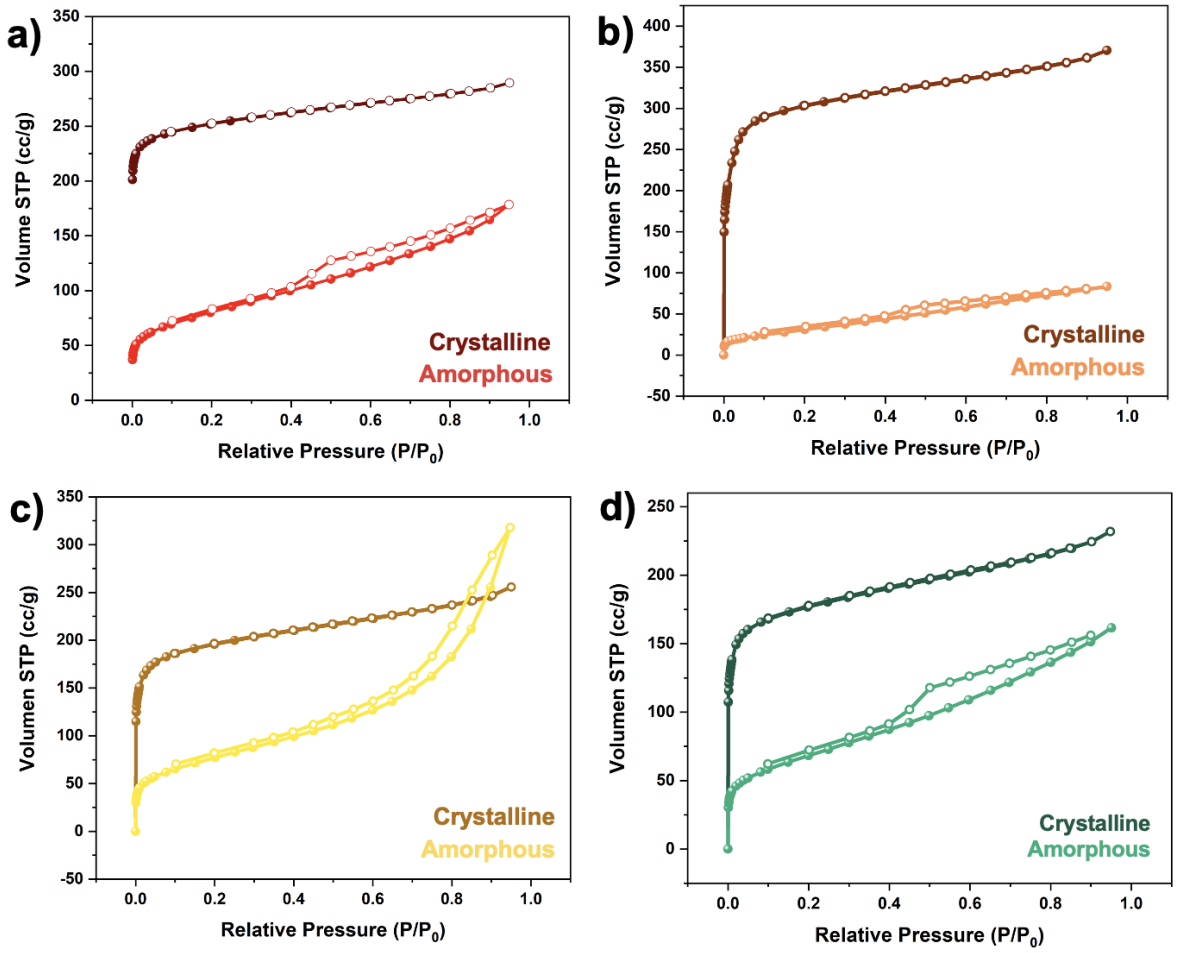

Figure S24: N_2 adsorption (open circles) and desorption (closed circles) isotherms at 77 K for crystalline (dark) and amorphous (light) a) UiO-66, b) UiO-66-NH_2, c) UiO-66-NO_2 and d) UiO-66-Cl.

Table S9: BET surface areas reported in literature for directly synthesised amorphous Zr-based MOFs.

Material	Linker	BET Surface Area (m^2/g)	Ref.
a_sUiO-66	BDC	286	This Work
a_sUiO-66-NH_2	BDC-NH_2	120	"
a_sUiO-66-NO_2	BDC-NO_2	277	"
a_sUiO-66-Cl	BDC-Cl	243	"
a_sUiO-66	BDC	17	14
a_sUiO-66	BDC	130	15
ZrATMP	ATMP*	80	16
a_sUiO-66-SO_3H	BDC-SO_3H	11**	17
SPUZ-1	icpp-1***	47	18
SPUZ-2	icpp-2***	59	"

*ATMP = Nitrilotrimethylene Triphosphoric Acid
**Collapse occurred *via* activation of the MOF material
***icpp = Porphyrin-based linkers

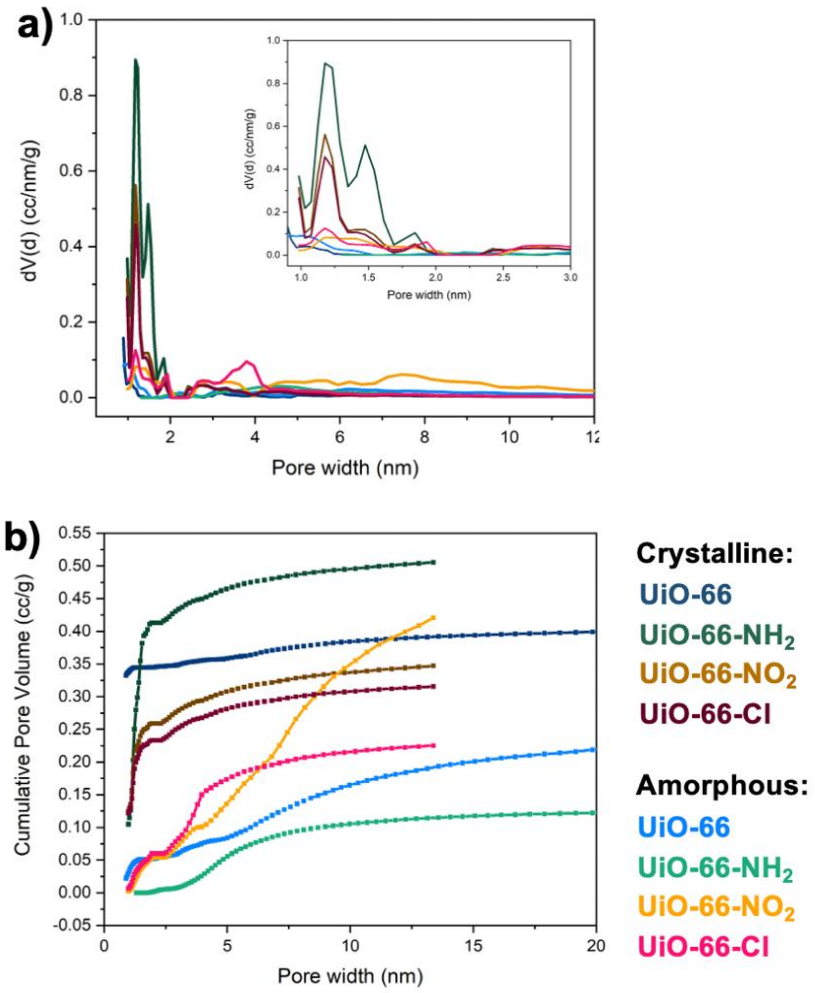

Figure S25: a) Pore width of Zr-MOF, inset zoomed in on nanopore region, and b) cumulative pore volume materials. Key shows the materials measured.

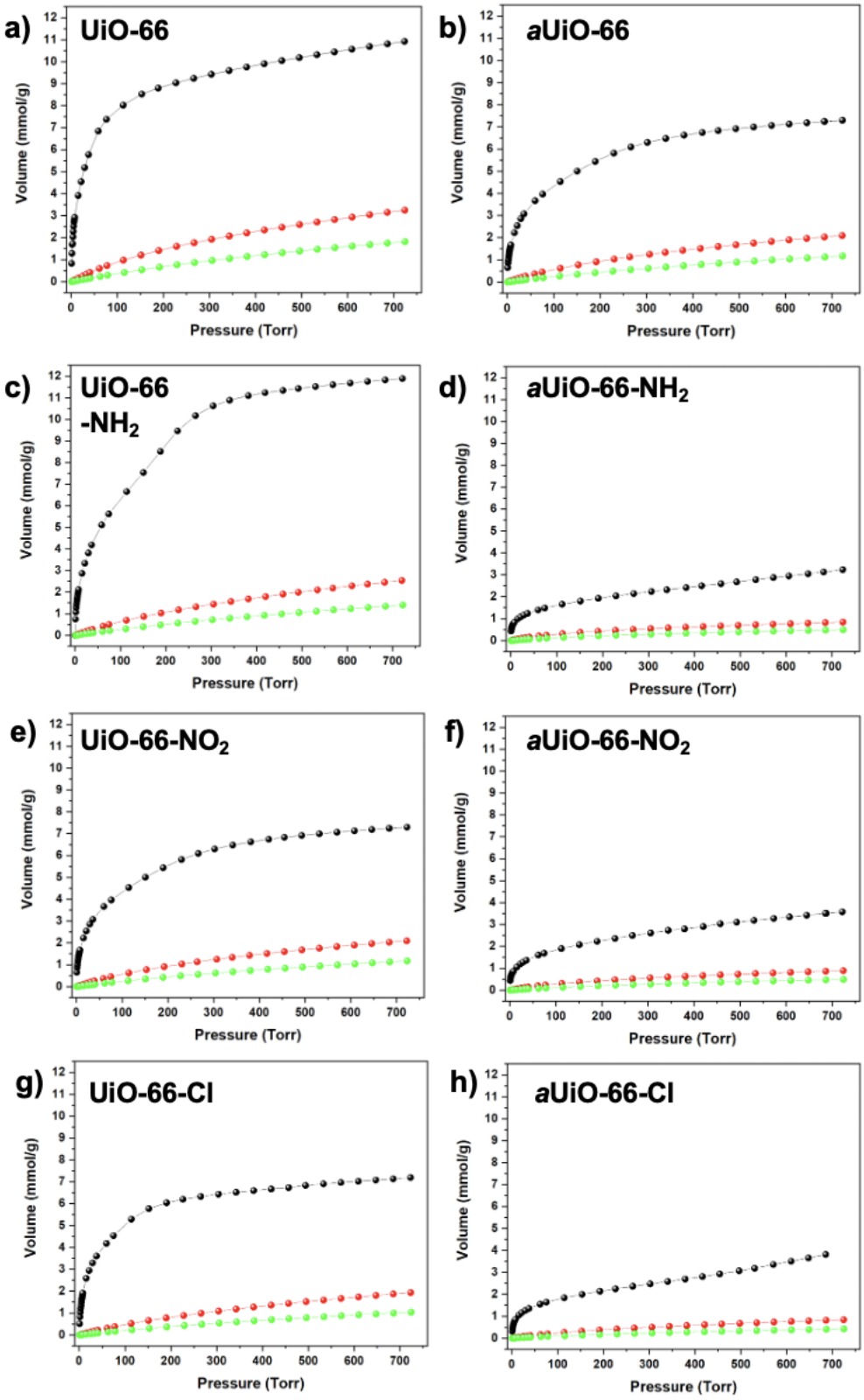

Figure S26: CO_2 adsorption isotherms collected at 195 K (acetone, dry ice) (black), 273 K (ice water) (red) and 298 K (green). a) UiO-66, b) *a*UiO-66, c) UiO-66-NH_2, d) *a*UiO-66-NH_2, e) UiO-66-NO_2, f) *a*UiO-66-NO_2, g) UiO-66-Cl, h) *a*UiO-66-Cl.

4.2. Catalytic Testing

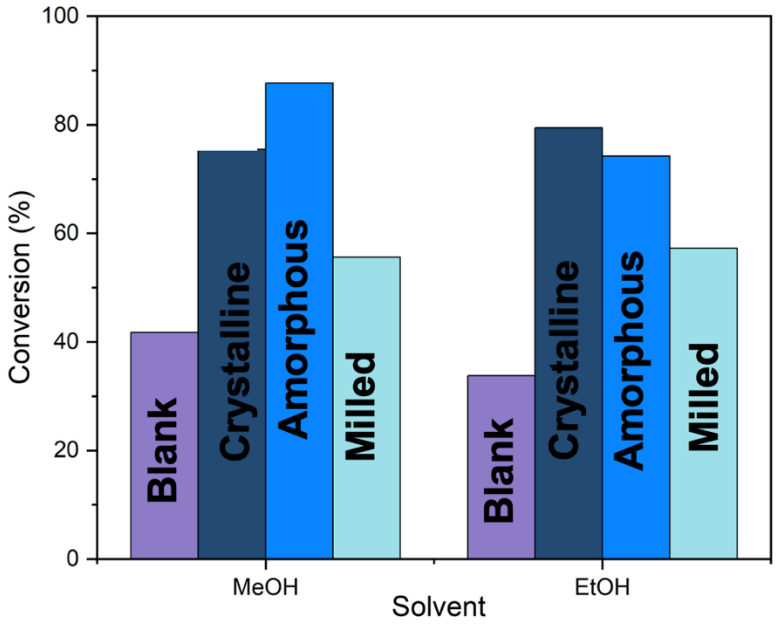

Figure S27: % Conversion for the esterification of Levulinic acid into methyl- or ethyl-levulinate. Conversion was extracted using gas chromatography.

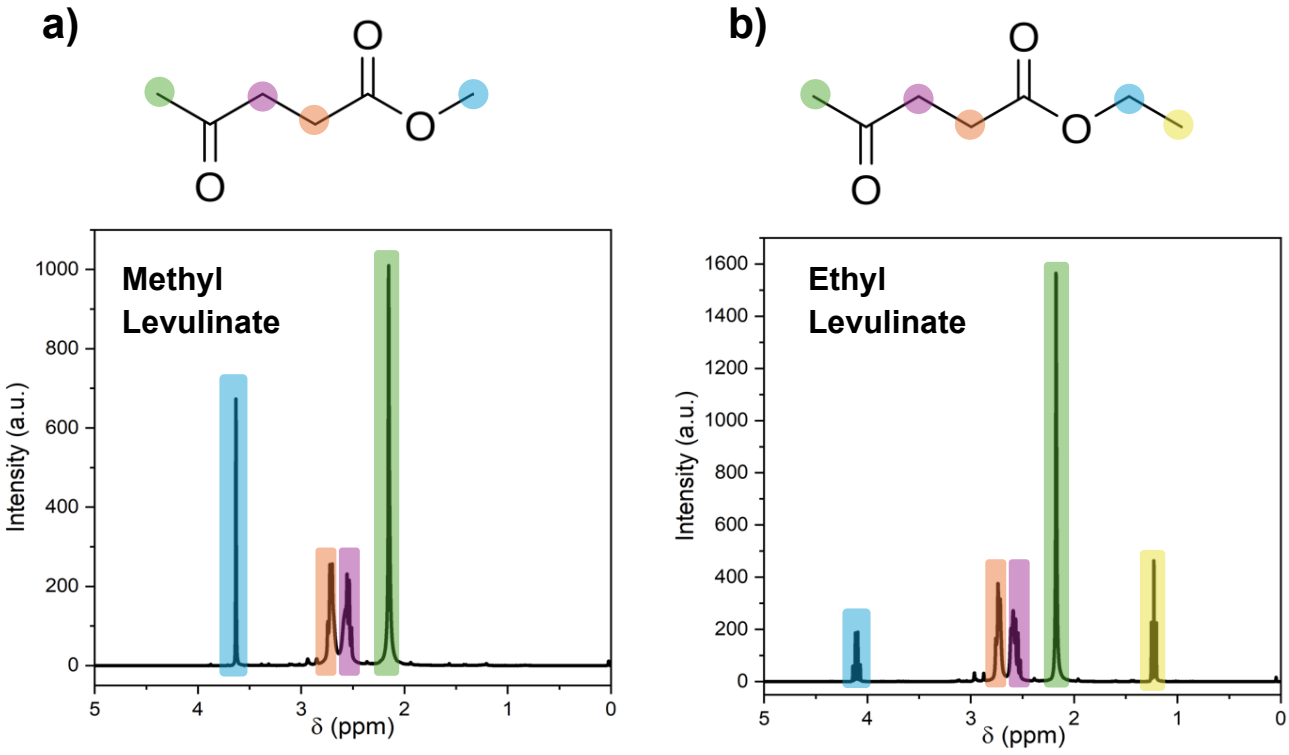

Figure S28: ^{1}H NMR, in $CDCl_3$, of the products of the UiO-66 catalysed esterification of leuvelinic acid to form a) methyl levulinate, b) ethyl levulinate.

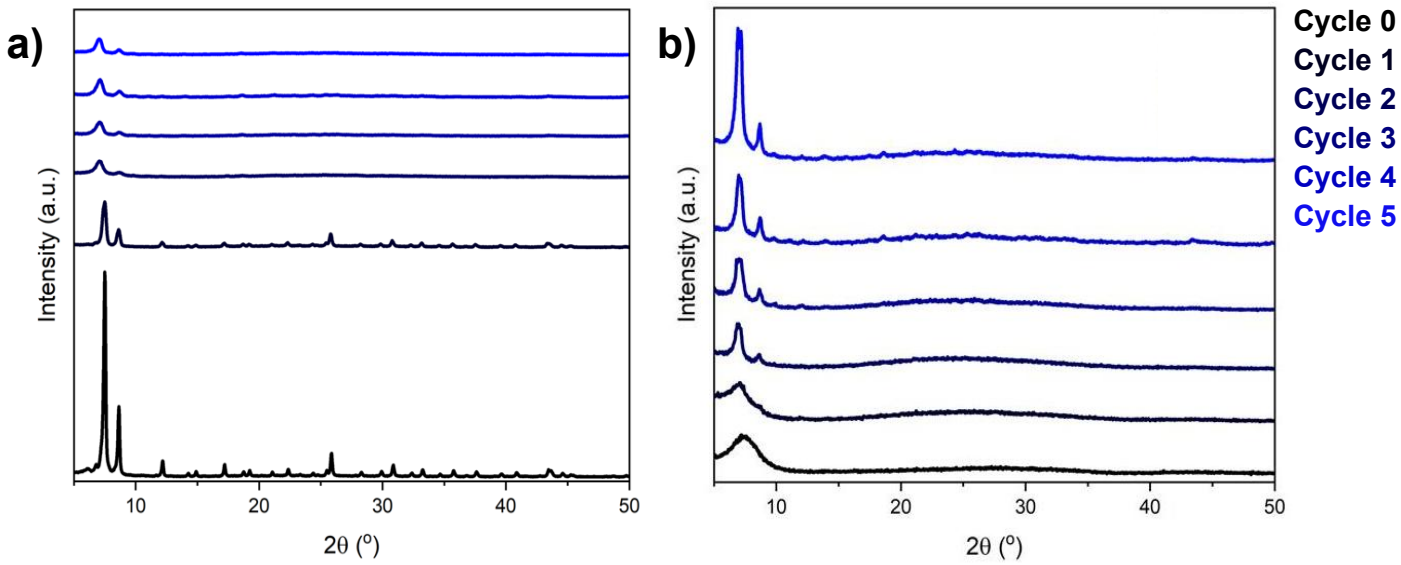

Figure S29: PXRD of a) crystalline and b) amorphous UiO-66 catalysts recovered after esterification reactions. Key shows the number of cycles of the catalysts.

Table S10: Catalytic results obtained for the esterification of Levulinic acid (LA) with Zr-based MOFs. Conversion by other heterogeneous catalysts has been outlined by Cirujano *et al*.[19]

Material	Alcohol	Conditions	Conversion (%)	Selectivity (%)	Ref.
UiO-66	MeOH	1% Cat., 120 °C, 3h, 1:5 LA:A	75	100	This Work
a_sUiO-66	MeOH	1% Cat., 120 °C, 3h, 1:5 LA:A	88	100	"
a_mUiO-66	MeOH	1% Cat., 120 °C, 3h, 1:5 LA:A	56	75	"
UiO-66	EtOH	1% Cat., 120 °C, 3h, 1:5 LA:A	79	100	"
a_sUiO-66	EtOH	1% Cat., 120 °C, 3h, 1:5 LA:A	75	100	"
a_mUiO-66	EtOH	1% Cat., 120 °C, 3h, 1:5 LA:A	57	100	"
UiO-66-NH_2	EtOH	1% Cat., 120 °C, 3h, 1:5 LA:A	61	100	"
a_sUiO-66-NH_2	EtOH	1% Cat., 120 °C, 3h, 1:5 LA:A	62	100	"
UiO-66-NO_2	EtOH	1% Cat., 120 °C, 3h, 1:5 LA:A	60	100	"
a_sUi-66-NO_2	EtOH	1% Cat., 120 °C, 3h, 1:5 LA:A	68	100	"
UiO-66-Cl	EtOH	1% Cat., 120 °C, 3h, 1:5 LA:A	54	100	"
a_sUiO-66-Cl	EtOH	1% Cat., 120 °C, 3h, 1:5 LA:A	59	100	"
UiO-66	MeOH	0,05g Cat., 1h, 130 °C, 30 barr, 1:15 LA:A	50	59	20
UiO-66-NH_2	MeOH	0,05g Cat., 1h, 130 °C, 30 barr, 1:15 LA:A	73	83	"
$ZrCl_4$	MeOH	0,05g Cat., 1h, 130 °C, 30 barr, 1:15 LA:A	98	100	"
UiO-66	EtOH	5% Cat., 78 °C, 4h, 1:5 LA:A	49	100	"
UiO-66	EtOH	5% Cat., 100 °C, 4h, 1:5 LA:A	73	100	19
UiO-66–NH_2	EtOH	5% Cat., 78 °C, 4h 1:15 LA:A	78	100	"
UiO-66–NH_2	EtOH	5% Cat., 78 °C, 8h 1:15 LA:A	95	100	"
UiO-66	EtOH	5% Cat., 78 °C, 4h 1:15 LA:A	78	100	"
UiO-66	EtOH	5% Cat., 78 °C, 8h 1:15 LA:A	94	100	"

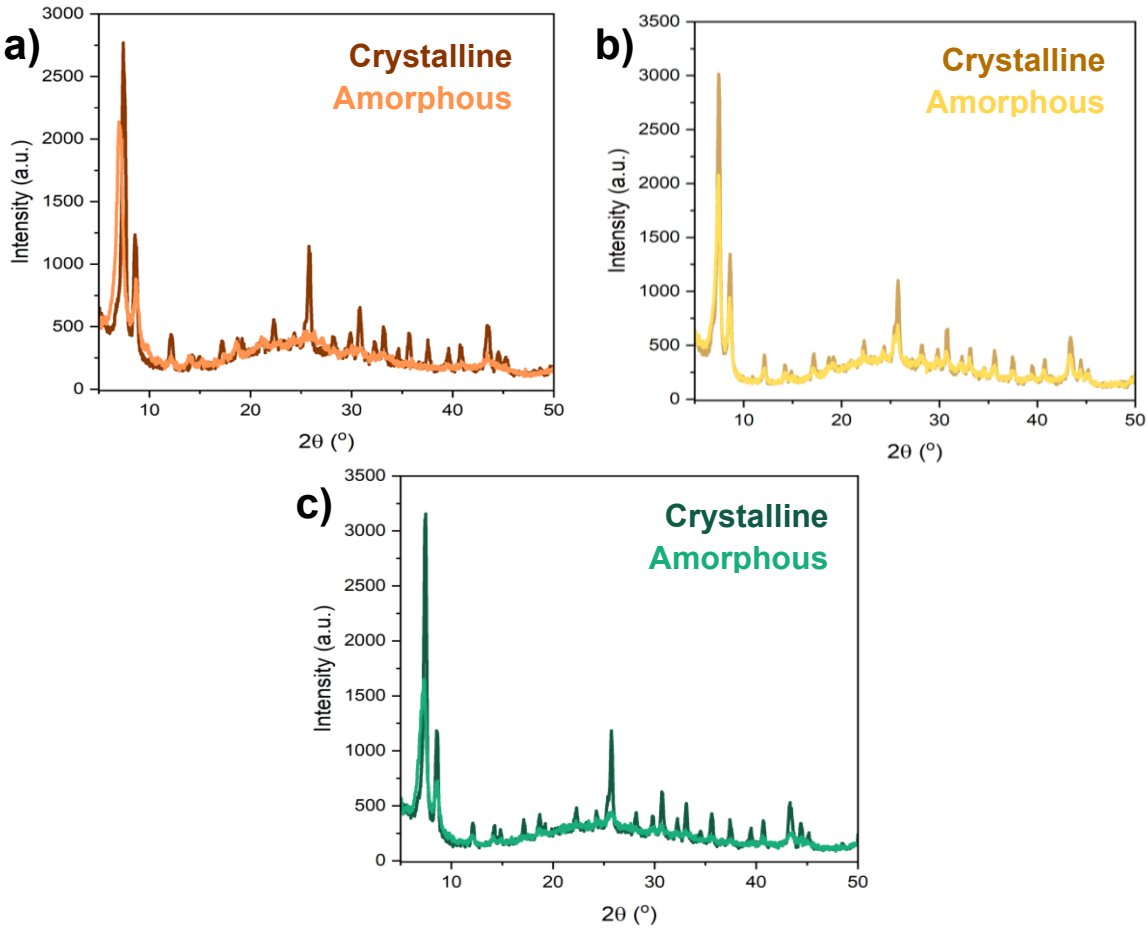

Figure S30: PXRD analysis of UiO-66, crystalline (dark) and amorphous (light), samples after 1 cycle of catalysis. a) UiO-66-NH_2, b) UiO-66-NO_2, and c) UiO-66-Cl.

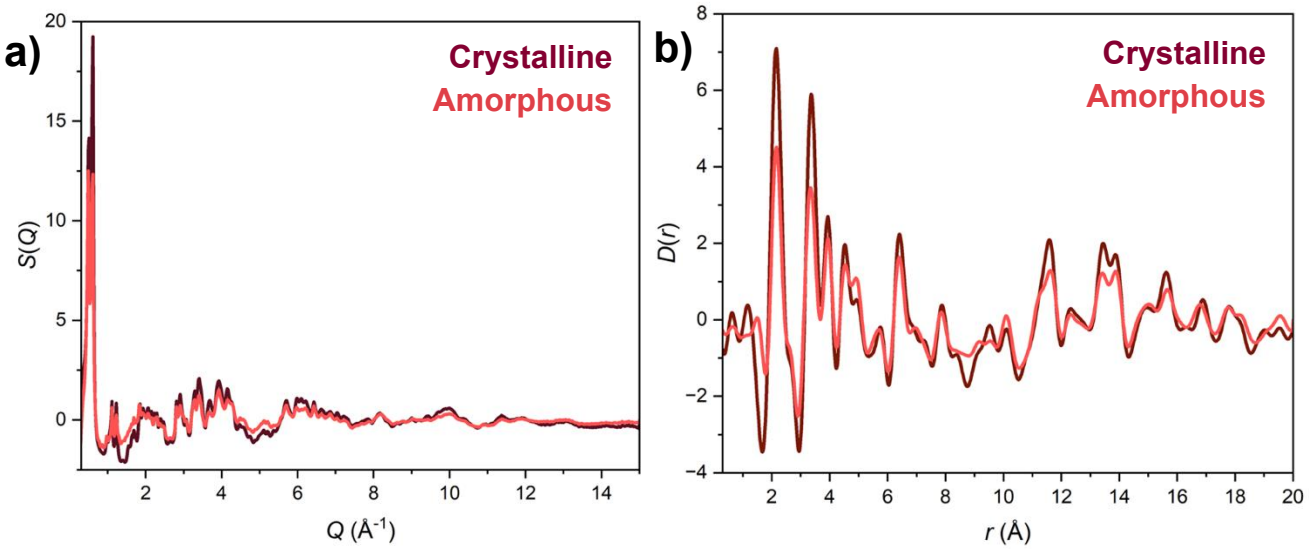

Figure S31: a) Total scattering data and b) PDF analysis of UiO-66 (dark red) and *a*UiO-66 (light red) after 5 catalytic cycles. Data were collected at I-151 beamline at Diamond Light Source (CY39316-1), wavelength = 0.161669 Å.

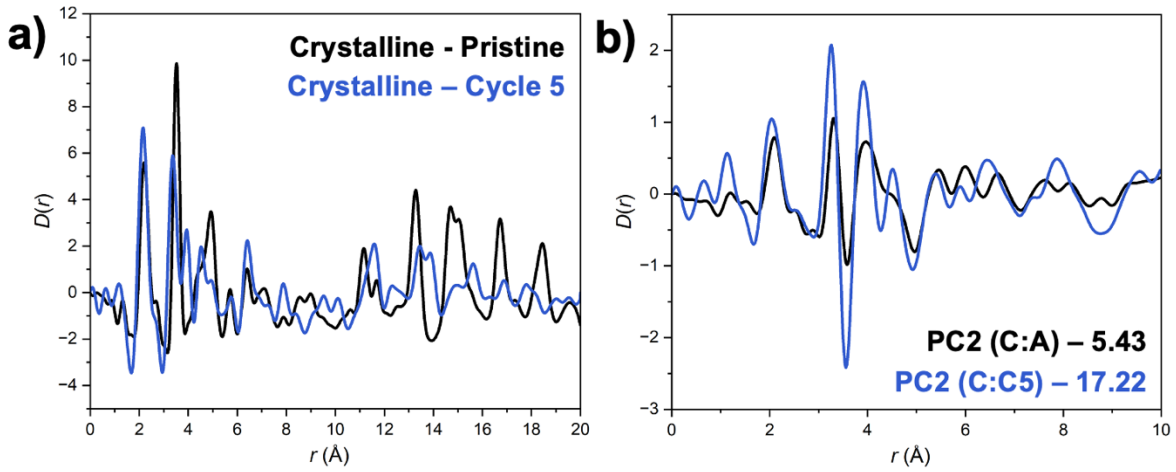

Figure S32: a) PDF analysis of crystalline UiO-66 before catalysis (black) and after 5 cycles of catalysis (blue). b) PC2 extracted from the principle component analysis of pristine crystalline and amorphous UiO-66 (black) and of pristine UiO-66 and UiO-66 after 5 cycles (blue). Data were cropped at 10 Å.

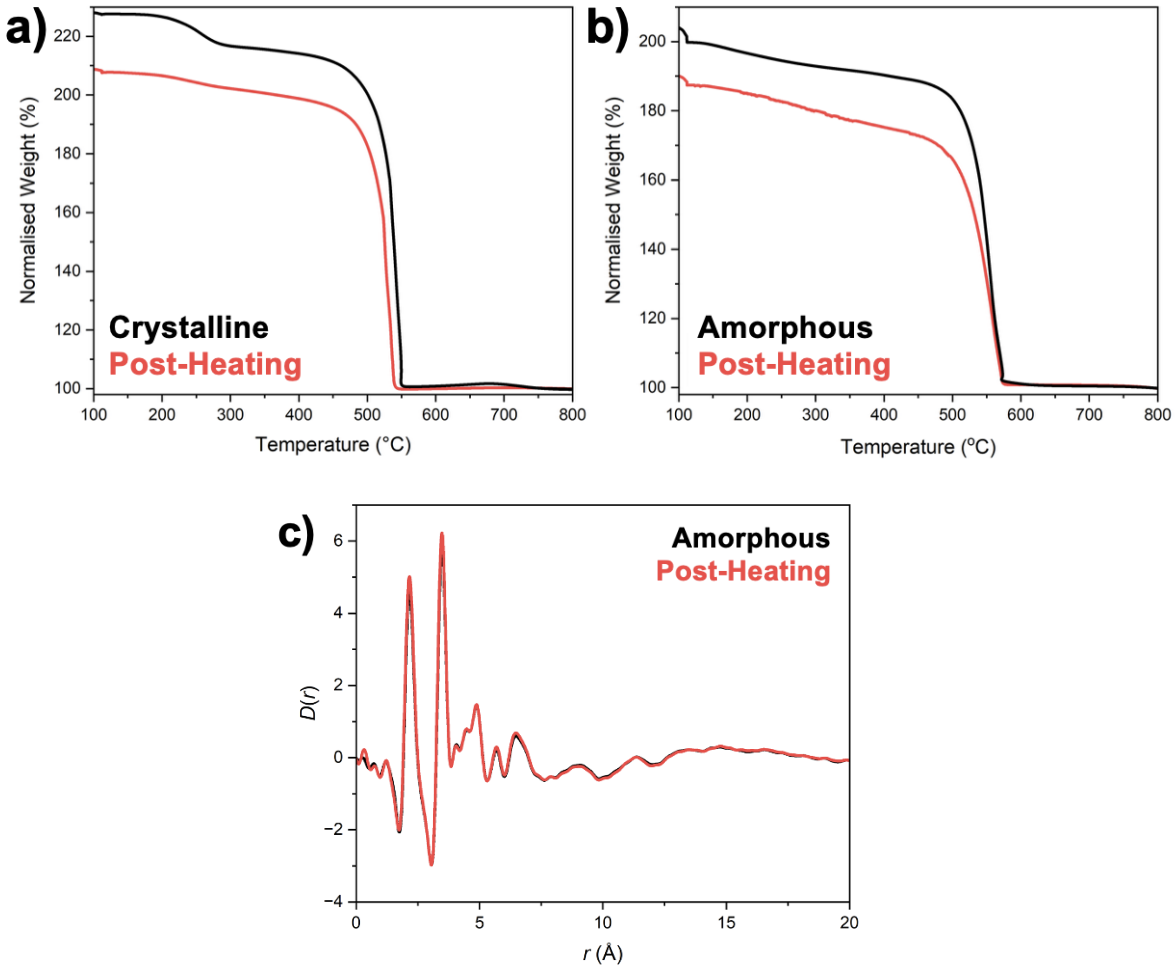

Figure S33: Analysis of UiO-66 prior (black) to and post (red) heating in EtOH. a) TGA of UiO-66, post heating for ~3h at 120 °C. b) TGA of a_sUiO-66, post heating for ~3h at 120 °C. c) PDF analysis of asUiO-66, post heating at 80 °C.

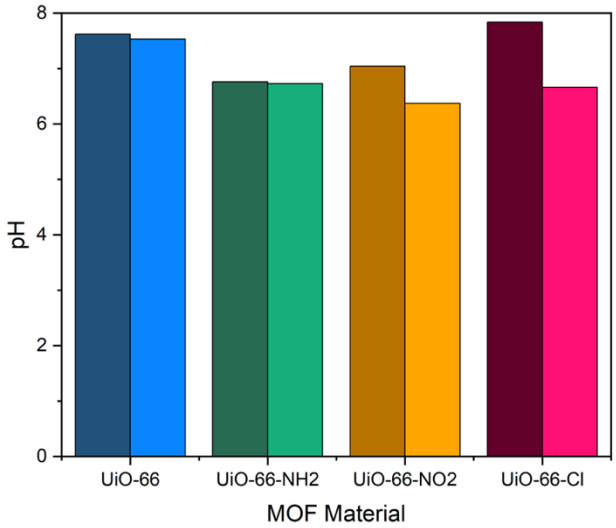

Figure S34: pH probe testing in MeOH of UiO-66-X materials, crystalline (dark) and amorphous (light). pH of MeOH was measured at 8.97.

Table S11: A summary of the structural analysis of crystalline and amorphous UiO-66 reported in this work.

Technique	Crystalline UiO-66	Amorphous UiO-66
PXRD	Sharp Bragg peaks, with fitting confirming literature-equivalent structure.	Broad Bragg features, consistent with post-synthetically amorphous UiO-66.
SED	Defined Bragg spots and rings, consistent with a polycrystalline sample.	Diffuse scattering across all investigated sample regions.
Total Scattering	Sharp Bragg peaks.	Broad features.
PDF - LRO	Long-range peak intensity consistent with a crystalline material.	Broad features consistent with cross-linking occurring, with no defined structural correlation.
PDF - SRO	Equivalent short-range order to that defined by the $Zr_6O_4(OH)_4$ cluster structure.	Shifts in the local structure consistent with the cluster structure retaining connectivity, but varying geometry, likely a distorted Zr-oxo cluster.
XPS	Consistent with literature environments.	Decreased number of Zr-O bonds, consistent with a loss of Zr-OH from the cluster, and decreased linker binding.
FTIR	Bound terephthalic acid linker peaks, and strong Zr-O stretching peak.	Presence of dicoordinated, monocoordinated and uncoordinated linker in the structure, with the broad linker peaks suggestive of disorder. Decreased intensity of Zr-O stretch.
Far-IR	Sharp peaks corresponding to cluster-based vibrations.	Broadening of Zr-O stretch, consistent with cluster disorder.
TGA	Weight-losses corresponding to dehydroxylation and linker decomposition.	Decreased weight-losses associated with dehydroxylation, suggestive of the loss of Zr-OH groups in the cluster, and linker decomposition, consistent with reduced Zr:linker ratio. Equivalent thermal decomposition temperature.
Porosity	Permeant porosity dominated by microporous structure.	Decreased porosity, relative to the crystalline material, whilst retaining a meso/macroporous regime.

5. References

1 M. J. Katz, Z. J. Brown, Y. J. Colón, P. W. Siu, K. A. Scheidt, R. Q. Snurr, J. T. Hupp and O. K. Farha, *Chemical Communications*, 2013, **49**, 9449.

2 G. P. Robertson, S. Mosca, C. Castillo-Blas, F. A. Son, O. K. Farha, D. A. Keen, S. Anzellini and T. D. Bennett, *Inorg. Chem.*, 2023, **62**, 10092–10099.

3 A. A. Coelho, *J. Appl. Crystallogr.*, 2018, **51**, 210–218.

4 D. Johnstone, P. Crout, C. Francis, M. Nord, J. Laulainen, S. Høgås, E. Opheim, E. Prestat, B. Martineau, T. Bergh, N. Cautaerts, H. W. Ånes, S. Smeets, V. J. Femoen, A. Ross, J. Broussard, S. Huang, S. Collins, T. Furnival, D. Jannis, I. Hjorth, E. Jacobsen, M. Danaie, A. Herzing, T. Poon, S. Dagenborg, R. Bjørge, A. Iqbal, J. Morzy, T. Doherty, T. Ostasevicius, T. I. Thorsen, M. von Lany, R. Tovey and P. Vacek, *Zenodo*, 2024, preprint, DOI: 10.5281/zenodo.11585254.

5 D. A. Keen, *Crystallogr. Rev.*, 2020, **26**, 143–201.

6 D. A. Keen, *J. Appl. Crystallogr.*, 2001, **34**, 172–177.

7 A. K. Soper and E. R. Barney, *J. Appl. Crystallogr.*, 2011, **44**, 714–726.

8 C. L. Farrow, P. Juhas, J. W. Liu, D. Bryndin, E. S. Božin, J. Bloch, T. Proffen and S. J. L. Billinge, *Journal of Physics: Condensed Matter*, 2007, **19**, 335219.

9 *Origin Lab, USA*, preprint, Origin Lab, USA:2023.

10 A. Nuhnen and C. Janiak, *Dalton Transactions*, 2020, **49**, 10295–10307.

11 F. G. Cirujano and F. X. Llabrés i Xamena, *J. Phys. Chem. Lett.*, 2020, **11**, 4879–4890.

12 M. Wojdyr, *J. Appl. Crystallogr.*, 2010, **43**, 1126–1128.

13 Y. Ma, X. Han, S. Xu, Z. Wang, W. Li, I. da Silva, S. Chansai, D. Lee, Y. Zou, M. Nikiel, P. Manuel, A. M. Sheveleva, F. Tuna, E. J. L. McInnes, Y. Cheng, S. Rudić, A. J. Ramirez-Cuesta, S. J. Haigh, C. Hardacre, M. Schröder and S. Yang, *J. Am. Chem. Soc.*, 2021, **143**, 10977–10985.

14 F. Yang, W. Li and B. Tang, *J. Alloys Compd.*, 2018, **733**, 8–14.

15 Y. Yin, C. Fan, L. Cheng and Y. Shan, *Food Chem. X*, 2024, **23**, 101555.

16 Y. Song, Q. Zhang, Y. Li and A. Tang, *Chemical Engineering Journal*, 2025, **522**, 167948.

17 Z. Hu, J. Lin, N. Ogiwara, A. Rodriguez, Y. Peng, Y. Wang, S. Horike and D. Zhao, *CrystEngComm*, 2016, **18**, 2803–2807.

18 W. Zuo, S. Yang, Y. Xing, X. Xiao, D. Fan, H. Li, G. Wang, B. Qin, S. You and X. Jia, *Dalton Transactions*, 2022, **51**, 6631–6637.

19 F. G. Cirujano, A. Corma and F. X. Llabrés i Xamena, *Chem. Eng. Sci.*, 2015, **124**, 52–60.

20 D. A. Bravo Fuchineco, A. C. Heredia, S. M. Mendoza, E. Rodríguez-Castellón and M. E. Crivello, *ChemEngineering*, 2022, **6**, 26.